

Dynamical evolution of boson stars: Perturbing the ground state

Edward Seidel

*Department of Physics, Washington University, St. Louis, Missouri 63130
and National Center for Supercomputing Applications, University of Illinois, Champaign, Illinois 61820**

Wai-Mo Suen

Department of Physics, Washington University, St. Louis, Missouri 63130

(Received 8 January 1990)

This is the first paper in a series in which we study the dynamical evolution of self-gravitating complex scalar field configurations (boson stars) in numerical relativity. Boson stars have equilibrium configurations corresponding to different levels of excitation of the scalar fields (i.e., different numbers of nodes). In this paper we report on the dynamical evolution of the perturbed ground-state boson stars. The major results are the following. (i) Under finite perturbations (with possibly finite changes in the total mass M and the particle number N), the ground-state configurations of a boson star consist of a stable branch and an unstable branch. The transition point corresponds to a critical mass of $M = 0.633(M_{\text{Planck}}^2/m)$, where m is the mass of the scalar field, depending slightly on the type of perturbation considered. This extends the previous result obtained by other authors that there are two such branches under infinitesimal perturbations with fixed M and N . (ii) The configurations on the stable branch, when perturbed, will oscillate, emit scalar field radiation with a characteristic frequency, and settle down into a new configuration with less mass and a larger radius than the initial perturbed configuration. The quasinormal frequency and the decay rate have been studied. The decay rate is an increasing function of the oscillation amplitude. (iii) The configurations on the unstable branch, when perturbed, either collapse to a black hole or migrate to and eventually settle down on the stable branch, depending on the type of perturbation. This behavior has been seen in initial configurations with both positive and negative binding energies. These results have implications on the actual existence and the formation of boson stars in an astrophysical environment.

I. INTRODUCTION

One of the most important implications of particle physics on cosmology and astrophysics is that bosonic particles might play a significant role in the evolution and the structure of the Universe. Although detailed models of these bosons have not been uniquely determined, there are both theoretically appealing reasons (e.g., for driving inflation¹) and observational suggestions (e.g., dark matter²) for studying these bosons seriously. Many particle theories predict the existence of weakly interacting bosons that are produced efficiently in the early Universe and are abundant in the present epoch. Studies of galaxy formation and primordial nucleosynthesis indicate that the dark matter is likely to be more abundant than baryonic matter,³ and there are suggestions that the dark matter could be made up of bosonic particles.⁴ This bosonic matter would condense through some sort of the Jeans instability to form compact gravitating objects. This is the reason for the recent surge of interest in astrophysical bosonic objects—boson stars. In this series of papers we study numerically the formation and dynamical evolution of boson stars in an astrophysical environment.

The simplest kind of boson star is made up of a complex scalar field.^{5–12} The equilibrium configurations are given by the soliton solutions of the Klein-Gordon scalar

field equation and the Einstein equations. These solutions are determined by the requirement that the metric quantities be static, though the complex scalar field ϕ must have a time-dependent phase factor so that $\phi(r, t) = \phi_0(r)e^{-i\omega_0 t}$. The lowest-energy solution (the ground-state boson star) has no nodes in the scalar field. It is a gravitationally bound state which is supported against collapse purely by the Heisenberg uncertainty principle. The excited state scalar field solutions have the number of nodes in the radial direction equal to the order of the excitation. A typical scalar field configuration for the ground state and first excited state are shown in Fig. 2. The mass of a boson star ranges from 10^{11} kg (Refs 5–7) (for noninteracting bosons with mass of the order of a GeV) to much greater than that of a neutron star (for self-interacting bosons; the mass of the star depends on the self-coupling⁶).

The similarity of a boson star in its ground state with a neutron star is particularly noteworthy. [The energy-density distributions of the excited state boson stars have a shell-like structure; but those of the ground state do not (see Fig. 2).] The mass profile of the ground-state star against its value of the scalar field at the center $\phi(0)$ has a peak with $M = 0.633(M_{\text{Planck}}^2/m) = 1.7 \times 10^{11}$ kg (for a scalar field mass m of 1 GeV) at $\phi(0)_c = 0.271$ [for ϕ defined as in Eq. (3.4)]. The mass profile is shown in Figs. 3(a) and 3(b). It has been shown by Gleiser and Wat-

kins¹¹ and Lee and Pang¹² that the ground-state equilibrium configurations with $\phi(0) < \phi(0)_c$ are stable with respect to infinitesimal perturbations with fixed total mass M and the total scalar particle number N , whereas for $\phi(0) > \phi(0)_c$ the configurations are unstable. This situation is exactly analogous to that of a neutron star.

In this paper we study the behavior of these ground-state equilibrium configurations under more general types of perturbations. For boson stars in an astrophysical environment (and indeed, in order to answer the question of whether or not they can exist in such an environment) we must study finite perturbations which may *change* the total mass M and the total particle number N (e.g., perturbations which correspond to more scalar particles or ordinary matter accreting onto the star, and the annihilation of the scalar particles through coupling to other fields). In this paper we follow the dynamical evolution of the boson stars under these perturbations, using the 3+1 formulation of general relativity. We restrict the treatment to spherically symmetric configurations in this paper.

The mathematical formulation of the problem and the numerical methods are described in Secs. II and III. We use a variant of the MacCormack scheme to evolve the spacetime with polar-sliced spatial hypersurfaces. The algorithm and the variables we use, the initial conditions, the boundary conditions, the comparison between codes we developed, various tests of accuracy, numerical stability, and results of convergence tests are described.

We find that the dynamical evolution of the perturbed star can be described well either by the radius R of the star or alternatively by the peak value of g_{rr} . (We define R by the radius containing 95% of the total mass, measured at infinity, as read out from the asymptotic form of the metric coefficient g_{rr} .¹³) Figure 3(b) for M versus R shows explicitly the similarity between the boson stars and neutron stars. The perturbations of the S branch, i.e., the configurations with $R > R_c$ [$\phi(0) < \phi(0)_c$] are discussed in Sec. IV B. In Fig. 6 we show the fundamental oscillation frequencies of boson stars versus their masses. These frequencies are obtained by considering very small perturbations. In the linear analysis, all modes of oscillation of stars on this branch are stable.^{11,12} We find that when the nonlinear interaction is considered, that is when the effect on the perturbation by the gravitational potential generated by the perturbation itself is taken into account, the oscillations are damped. This damping can be seen in Fig. 5. Furthermore, the nonlinear effect causes the oscillation frequencies to lie below the fundamental oscillation frequencies. The change in mass versus oscillation frequencies for nonlinear oscillations is shown in Fig. 6. This figure enables us to estimate the end-point configurations resulting from various kinds of perturbations, which are discussed in Secs. IV B and IV C. The fact that the oscillations are damped, and that the boson stars on this branch can return to an equilibrium configuration with lower total mass and a larger radius is nontrivial: since the system is spherically symmetric (no gravitational waves may be emitted) and the scalar field satisfies the Klein-Gordon equation (which contains no viscous terms), the only mechanism for the

system to return to an equilibrium state is through the radiation of the scalar field. This mechanism is central to the initial condensation and formation of a boson star. We study this mechanism in terms of the Newtonian limit of the relativistic system in Sec. IV B.

In Sec. IV C we study the perturbations of the boson-star configurations in the U branch, i.e., configurations with $R < R_c$ [i.e., $\phi(0) > \phi(0)_c$]. We find that the generic evolution is that when the star is perturbed to the left of the equilibrium line in the M - R diagram [cf. Fig. 3(b)] corresponding to the total mass M of the star being perturbed to a higher value due to additional matter falling in, or alternatively due to a fluctuation to a smaller radius, a collapse is triggered. In this process the star will fall through its horizon, generally with an insignificant amount of scalar radiation to infinity. In the runs we performed, the mass radiated is generally less than 0.1% of the total mass of the boson star. When the star is perturbed to the other side of the equilibrium line in the M - R diagram, corresponding to an annihilation of scalar particles due to some coupling to other fields, or by a fluctuation to a larger radius, the star initially expands in radius. However, it will then fall back in size after it crosses the S branch of the equilibrium line in the M - R diagram [Fig. 3(b)], sending out a burst of scalar radiation to infinity. The remaining boson star core will oscillate and settle down to a new equilibrium configuration on the S branch with a smaller mass. This migration process is independent of whether the initial configuration has $E = M - Nm$ positive or negative (where m is the mass of the scalar particle, M is the boson star mass, and N is the particle number). That is, at least some configurations with excess energy (i.e., negative binding energy) manage to radiate enough scalar radiation to form a stably bound ground-state star for the perturbations we have considered. This migration process has important implications on the formation of boson stars through a “Jeans instability.”

In Sec. IV D we study perturbations of configurations near the transition point $R = R_c$ [$\phi(0) = \phi(0)_c$]. This is an exact transition point under infinitesimal perturbations with fixed mass M and particle number N .^{11,12} The primary conclusion of this subsection is that for general perturbations, the notion of this transition point is no longer exact, but the $R_c, \phi(0)_c$ point remains as a useful characterization of the transition from stable to unstable boson stars. The results are summarized in Sec. V.

II. MATHEMATICAL FOUNDATIONS

A self-gravitating complex scalar field system in general relativity is described by the action

$$I = \frac{1}{16\pi G} \int d^4x \sqrt{-g} R - \int d^4x \left[\sqrt{-g} \left(\frac{1}{2} g^{\mu\nu} \partial_\mu \Phi^* \partial_\nu \Phi + \frac{1}{2} m^2 \Phi^* \Phi + \frac{1}{4} \lambda |\phi|^4 \right) \right]. \quad (2.1)$$

This leads to the scalar field equation

$$g^{\mu\nu}\phi_{;\mu\nu} - m^2\phi - \lambda(\phi^*\phi)\phi = 0, \quad (2.2)$$

and the Einstein field equations

$$R_{\mu\nu} - \frac{1}{2}g_{\mu\nu}R = 8\pi GT_{\mu\nu}, \quad (2.3)$$

where

$$T_{\mu\nu} = \frac{2}{\sqrt{-g}} \frac{\partial}{\partial g^{\mu\nu}} [L_M], \quad (2.4)$$

with the matter Lagrangian density L_M given by the terms in the square brackets in Eq. (2.1). Equations (2.2)–(2.4) completely determine the scalar field $\phi(x, t)$ and the metric up to certain coordinate choices to be discussed below, once appropriate initial conditions and boundary conditions are specified. Unlike the case of an ordinary star, there is no need to specify an equation of state; all information about the interactions between particles is provided directly by the action in Eq. (2.1).

The metric for a spherically symmetric spacetime can be written in the form

$$ds^2 = -(N^2 - S^2)dt^2 + 2S dt dr + g^2 dr^2 + r^2 d\Omega^2, \quad (2.5)$$

where g , the lapse function N , and the shift S are functions of (t, r) and r is the circumferential radius. [We reserve t, r for the dimensionless rescaled quantities given in Eq. (3.4).] Within this coordinate choice we still have freedom in choosing N and S . Most of the results reported in this paper are obtained using the polar-slicing condition,¹⁴ which requires $K_{00} + K_{\phi\phi} = 0$ where K is the extrinsic curvature of a constant t slice in the metric Eq. (2.5). In the present spherically symmetric case, this implies the shift $S(t, r) = 0$. In our study, the most important consequence of the polar-slicing condition is that the

lapse function N decreases rapidly when an apparent horizon is approached (if there is one in the spacetime), so that no crossing of an apparent horizon is possible. For a review of the polar-slicing and other time-slicing conditions, see Bardeen and Piran.¹⁴

We have developed numerical codes both with and without a shift vector, and the two codes give results agreeing to high accuracy for all the tests we have run. In this paper we are interested mainly in the spacetime region away from the horizon (when there is one), and we used mainly the polar-slicing code. We believe that the code with the shift vector shows promise in obtaining late time behavior near the presence of a horizon. This shift vector code will be further developed and reported elsewhere. In the rest of this paper, we restrict ourselves to the case $S=0$.

For the metric (2.5) with $S=0$, the scalar field Eq. (2.2), is explicitly in terms of metric functions,

$$-\frac{1}{N^2} \left[\ddot{\Phi} - \frac{\dot{N}}{N} \dot{\Phi} - \frac{NN'}{g^2} \Phi' \right] + \frac{1}{g^2} \left[\Phi'' - \frac{g'}{g} \Phi' - \frac{gg'}{N^2} \Phi \right] + \frac{2\Phi'}{rg^2} - m^2\Phi = 0, \quad (2.6)$$

where $' \equiv \partial/\partial r$ and $\dot{\cdot} \equiv \partial/\partial t$. We have set $\lambda=0$ in (2.6), as in the rest of this paper. We will return to self-interacting case $\lambda \neq 0$ in a future publication in the series. Since the metric functions are real, both the real and imaginary parts of $\Phi = \Phi_1(r, t) + i\Phi_2(r, t)$ satisfy this equation.

In terms of Φ_1 and Φ_2 , the rr component of the Einstein equation is

$$N' = \frac{1}{2}N \left[\frac{g^2 - 1}{r} + 4\pi G r \left[((\Phi_1')^2 - g^2 m^2 \Phi_1^2) + ((\Phi_2')^2 - g^2 m^2 \Phi_2^2) + \frac{g^2}{N^2} (\dot{\Phi}_1^2 + \dot{\Phi}_2^2) \right] \right]. \quad (2.7)$$

This equation is an ordinary differential equation for the lapse function N , which can be solved on each time slice once the other quantities are known there. The numerical scheme for solving this equation is discussed in Sec. III. There is a similar ordinary differential equation for the radial metric function g , namely, the Hamiltonian constraint equation $G_{tt} - 8\pi GT_{tt} = 0$:

$$g' = \frac{1}{2} \left[4\pi G \left\{ g^3 r \frac{\dot{\Phi}_1^2 + \dot{\Phi}_2^2}{N^2} + rg(\Phi_1')^2 + rg(\Phi_2')^2 + rg^3 m^2 (\Phi_1^2 + \Phi_2^2) \right\} - \frac{g(g^2 - 1)}{r} \right]. \quad (2.8)$$

However, instead of solving (2.8) on each time slice for g , which is time consuming computationally, we have chosen to use this constraint equation as an independent measure of the accuracy of our numerical solution. We obtain the time development of $g(t, r)$ using the t, r component of Einstein equations:

$$\dot{g} = 4\pi G rg (\dot{\Phi}_1 \Phi_1' + \dot{\Phi}_2 \Phi_2'). \quad (2.9)$$

Equations (2.6), (2.7), and (2.9) form a complete set of equations for the four unknown functions Φ_1 , Φ_2 , N , and g . Before we go on to discuss the numerical technique for solving these equations, we first derive the Newtonian

limit of these equations. The Newtonian limit is useful for three reasons: (i) The Newtonian equations can be solved numerically free from the problems associated with choice of slicing and the violation of the Hamiltonian constraint. It provides a useful check to the relativistic code applied to weak gravity situations. (ii) The Newtonian equations are much simpler. The scalar field satisfies the familiar Schrödinger equation. This has great advantage in providing an intuitive understanding of the system (see Sec. IV B 2). (iii) The Newtonian analysis is particularly useful for studying the initial formation phase of the boson star where only weak gravity is involved. The results of an investigation of the formation of boson stars will be reported in a future publication in this series.

We obtain the Newtonian limit through the standard post-Newtonian expansion.¹⁵ We let the mass m of the scalar field be a quantity of order 1, whereas the wave number k of the Fourier spectrum of the field is only of order ϵ . Then the corresponding frequency

$$\omega = (k^2 + m^2)^{1/2}, \quad (2.10)$$

can be expanded as

$$\omega \approx m + \frac{1}{2}k^2m + O(\epsilon^4). \quad (2.10a)$$

Hence,

$$\partial_t \Phi \approx O(\epsilon)$$

and

$$\partial_t \Phi \approx m \Phi + O(\epsilon^2). \quad (2.11)$$

The energy associated with the scalar field is moving with a velocity

$$v \sim \frac{\partial \omega}{\partial k} \approx O(\epsilon). \quad (2.12)$$

The gravitational potentials $(N^2 - 1)$ and $(g^2 - 1)$ are of order

$$\frac{1}{r} \sim v^2 \approx O(\epsilon^2). \quad (2.13)$$

We let

$$\begin{aligned} N^2(\mathbf{t}, \mathbf{r}) &= 1 + \epsilon^2 V(\mathbf{t}, \mathbf{r}) + O(\epsilon^4), \\ g^2(\mathbf{t}, \mathbf{r}) &= 1 + \epsilon^2 U(\mathbf{t}, \mathbf{r}) + O(\epsilon^4). \end{aligned} \quad (2.14)$$

Derivatives of the geometric quantities are of order

$$\begin{aligned} \frac{\partial N^2}{\partial t} &\sim \frac{\partial g^2}{\partial t} \sim \epsilon^2 \frac{v}{r} V = O(\epsilon^5), \\ \frac{\partial N^2}{\partial t} &\sim \frac{\partial g^2}{\partial t} \sim \epsilon^2 \frac{1}{r} V = O(\epsilon^4). \end{aligned} \quad (2.15)$$

To separate out the positive-energy component of the Klein-Gordon field Φ [Eq. (2.2) with $\lambda=0$], we let

$$\Phi = e^{-imt} \tilde{\Phi}(x, t). \quad (2.16)$$

It is then straightforward to obtain from (2.6)–(2.9), to the leading nontrivial order in ϵ , the equations

$$i\dot{\tilde{\Phi}} = -\frac{1}{2m} \frac{1}{r} \frac{\partial^2}{\partial r^2} (r\tilde{\Phi}) + mV\tilde{\Phi}, \quad (2.17)$$

$$\frac{1}{r} \frac{\partial^2}{\partial r^2} (rV) = 4\pi G m^2 \tilde{\Phi} \tilde{\Phi}^*. \quad (2.18)$$

Equation (2.17) is the Schrödinger equation with $\hbar=1$, in a Newtonian potential $V(\mathbf{t}, \mathbf{r})$ generated by the Schrödinger field $\tilde{\Phi}$ itself through the Poisson equation (2.18).

To see that the source term in (2.18) is exactly what we expected, we note that due to the global U(1) symmetry $\Phi \rightarrow e^{i\alpha} \Phi$ of the action (2.1), there is a conserved current

$$J^\mu = \frac{i}{2} g^{\mu\nu} (\Phi_{,\nu}^* \Phi - \Phi_{,\nu} \Phi^*) \quad (2.19)$$

and an associated conserved charge, namely, the number of scalar particles on a constant t slice:

$$N_p = \int d^3x \sqrt{-g} J^t. \quad (2.20)$$

It is a conserved quantity if the spatial integration is over all space. In the Newtonian limit, (2.20) reduces to, in terms of the Schrödinger field $\tilde{\Phi}$,

$$N_p = m \int 4\pi r^2 d\mathbf{r} (\tilde{\Phi} \tilde{\Phi}^*). \quad (2.21)$$

Hence the source of the Newtonian potential V in (2.18) is simply $4\pi G m n$, with n being the number density of Schrödinger particles.

III. NUMERICAL TECHNIQUES

A. Numerical algorithm

The basic equations for the relativistic system are Eq. (2.6) for the scalar field variables Φ_1 and Φ_2 , Eq. (2.9) for g , and Eq. (2.7) for \mathbf{N} . Equation (2.7) is a first-order ordinary differential equation to be integrated on each time slice for the lapse function \mathbf{N} . Equations (2.6) and (2.9) are nonlinear partial differential evolution equations. They are solved using a modified MacCormack predictor-corrector scheme.¹⁶ We illustrate this scheme with Eq. (2.9) for g . In a predictor loop, a future value for g , denoted g_p , is “predicted” using data on the present n th slice

$$g_p^{(n+1)} = g^{(n)} + dt [4\pi G r g^{(n)} (\dot{\Phi}_1 \Phi_1' + \dot{\Phi}_2 \Phi_2')^{(n)}]. \quad (3.1)$$

Likewise the “predicted” values $\Phi_1^p, \Phi_1^p, \Phi_2^p, \Phi_2^p$ are obtained. Then the “predicted” value of \mathbf{N} is obtained by integrating Eq. (2.7) inward from the outer edge of the spatial grid to the origin, using the other “predicted” values. Next the corrected value of g on the $n+1$ slice is obtained using

$$\begin{aligned} g^{(n+1)} &= \frac{1}{2} \{ g_p^{(n+1)} + g^{(n)} \\ &\quad + dt [4\pi G r g_p^{(n+1)} (\dot{\Phi}_1^p \Phi_1^p + \dot{\Phi}_2^p \Phi_2^p)^{(n+1)}] \}. \end{aligned} \quad (3.2)$$

Likewise the corrected values $\Phi_1, \Phi_1, \Phi_2, \Phi_2$ on the $n+1$

slice are obtained. We integrate Eq. (2.7) inward once again using the corrected values to obtain \mathbf{N} . The spatial integration for the lapse function \mathbf{N} is performed on each time slice using a fourth-order Runge-Kutta method. This method requires that we provide data at the midpoint between grid points. These data are obtained using cubic spline interpolation.

The spatial derivative scheme we use in our code is different from what is normally used in the MacCormack method,¹⁶ namely, forward/backward differencing. We find that centered differencing works better in our problem. We have also tried spatial derivative schemes with various orders of accuracy. Lower-order derivative schemes are more stable but less accurate, requiring finer grids to keep the Hamiltonian constraint sufficiently satisfied. In the actual runs we use fourth- and sixth-order schemes, and we have checked extensively that the two codes with different schemes produce results which agree with each other to high accuracy. One example of this comparison is shown in Fig. 10(b).

We evolve the system of equations using equally spaced time steps dt . The proper time advance at each point is determined by the requirement of polar slicing. For higher accuracy and stability, we use a time step much smaller than the grid size. We find that when a small time step is used, the MacCormack code we use is significantly more accurate than staggered leapfrog and extrapolated leapfrog. An improvement of our code so that a larger time step can be used will be discussed elsewhere.

B. Eigenvalue problem for equilibrium models

In this subsection, for setting up the notation and for completeness, we briefly outline the construction of equilibrium configurations to which we apply perturbations. Equilibrium configurations have been obtained by other authors.⁵⁻⁷ By equilibrium configurations, we mean those configurations in which the metric is time independent. There is no solution in which the scalar field Φ is time independent. Instead, Φ must oscillate with a fixed frequency ω_0 :

$$\Phi(\mathbf{t}, \mathbf{r}) = \Phi_0(\mathbf{r}) e^{-i\omega_0 t}. \quad (3.3)$$

However, the energy-momentum tensor of the field given by (3.3) is time independent. We express the set of equations for the equilibrium configurations in terms of the following dimensionless rescaled quantities

$$r \equiv m \mathbf{r}, \quad t = \omega_0 \mathbf{t}, \quad \phi = \sqrt{4\pi G} \Phi, \quad N \equiv \mathbf{N} \frac{m}{\omega_0}. \quad (3.4)$$

These rescaled quantities are the primary variables we use for discussion throughout the paper. The Einstein equations in the equilibrium case in terms of these variables are

$$\phi'_0 = \Lambda,$$

$$\Lambda' = - \left[\frac{1}{r} + \frac{g^2}{r} - r g^2 \phi_0^2 \right] \Lambda - \left[\frac{1}{N^2} - 1 \right] \phi_0 g^2, \quad (3.5)$$

$$g' = \frac{1}{2} \left[\frac{g}{r} - \frac{g^3}{r} + \phi_0^2 r g^3 \left(1 + \frac{1}{N^2} \right) + r g \Lambda^2 \right],$$

$$N' = \frac{1}{2} \left[-\frac{N}{r} + \frac{N g^2}{r} + \frac{r g^2 \phi_0^2}{N} (1 - N^2) + r N \Lambda^2 \right],$$

where $\phi_0 \equiv \Phi_0 \sqrt{4\pi G}$. As in the rest of this paper, here a prime denotes $\partial/\partial r$ and an overdot denotes $\partial/\partial t$. Regularity at $r=0$ requires that $g(r=0)=1$ and that all other quantities are finite at $r=0$. For the solution to represent an isolated star, we require $\phi(r=\infty)=0$. For each choice of $\phi(r=0)$, the set of Eqs. (3.5) has a solution only when $N(r=0)$ takes on certain values. Different eigenvalues correspond to different numbers of nodes in the solution of $\phi(r)$. In Fig. 2 in the next section, a typical solution with no nodes (ground state) and a solution with one node (first excited state) are shown. In this paper we concentrate on the nodeless ground-state solution.

These equations are integrated numerically using either a fourth-order Runge-Kutta method or the DIVPRK routine from the International Mathematical and Scientific Library (IMSL10), with identical results. Operationally, we choose a central value of the scalar field, and integrate out to large radii for different values of $N(r=0)$ until the boundary conditions are satisfied.

C. Evolution equations

Equations (2.6), (2.7), and (2.9) above are not in optimal form for numerical solution. As is often the case, analytically equivalent set of equations may be more or less suited to accurate numerical evolution. In the present case, after some experimentation, we have chosen the following set of variables for the numerical evolution. We define

$$\psi_1 \equiv r \phi_1, \quad \psi_2 \equiv r \phi_2, \quad \pi_1 \equiv \frac{1}{\alpha} \frac{\partial \psi_1}{\partial t}, \quad \pi_2 \equiv \frac{1}{\alpha} \frac{\partial \psi_2}{\partial t}, \quad (3.6)$$

where

$$\alpha \equiv \frac{N}{g}.$$

In terms of these variables [and those in (3.4)], Eqs. (2.6), (2.7), and (2.9) become

$$\dot{g} = N (\pi_1 \phi'_1 + \pi_2 \phi'_2), \quad (3.7)$$

$$N' = \frac{N}{2} \left[\frac{g^2 - 1}{r} + r [(\phi'_1)^2 + (\phi'_2)^2 - g^2(\phi_1^2 + \phi_2^2)] + \frac{\pi_1^2 + \pi_2^2}{r} \right], \quad (3.8)$$

$$\dot{\pi}_i = \alpha' \psi'_i + \alpha \psi''_i - \psi_i \left[gN + \frac{\alpha'}{r} \right], \quad i = 1, 2, \quad (3.9)$$

$$\dot{\psi}_i = \alpha \pi_i, \quad i = 1, 2, \quad (3.10)$$

and (2.8) can be written

$$\frac{2g'}{rg^3} + \frac{g^2-1}{r^2g^2} - \frac{\pi_1^2+\pi_2^2}{r^2g^2} - \frac{\phi_1'^2+\phi_2'^2}{g^2} - (\phi_1^2+\phi_2^2) = 0. \quad (3.11)$$

Equations (3.4)–(3.10) are the actual set of equations evolved in our numerical code. In the following two sections we discuss the initial conditions and boundary conditions for the equations.

D. Perturbing initial data

We study the dynamics of the boson stars by perturbing the equilibrium configurations constructed in Sec. III B. There are two broad types of perturbations we considered. The first type changes the field distribution (ψ_1 and ψ_2) from its equilibrium structure. The effect of the accretion of scalar particles by the equilibrium star can be simulated by increasing the field distributions in the outer region of the star, while the effect of the annihilation of the scalar particles through coupling to other fields can be simulated by decreasing the field distributions in the denser region of the star. The perturbations are prescribed by, e.g., adding to ψ_1 an adjustable Gaussian-like distribution $\delta\psi_1$ in the designated region of the star. The height, width, and region of perturbation can be chosen arbitrarily. Once this choice has been made we recompute the metric functions g and N on the initial slice so that the initial constraint is satisfied and that the initial slice is a polar slice. This is done by integrating (3.8) and (3.11) on the initial slice.

The accretion of more scalar particles can change not only the rest energy density of the star but also the kinetic energy density distribution. In the second type of perturbation we simulate the change of the kinetic energy density distribution by changing the $\dot{\psi}_1$ and $\dot{\psi}_2$ of the equilibrium configuration. Since the scalar field equations are second order, the initial values of $\dot{\psi}_1$ and $\dot{\psi}_2$ can be changed independent of the changes made in ψ_1 and ψ_2 . The changes in the metric functions g and N on the initial slice are again determined by the initial constraint and the polar-slicing condition.

It is clear that perturbations prescribed this way are not necessarily small, nor do they have to keep the total mass or total number of scalar particles the same, although we can arrange for such particular cases. In this paper we do not consider the effect of accretion of ordinary matter into a boson star.

E. Boundary conditions

We have to supply boundary conditions at both $r=0$ and at the end of the grid at large r for the Eqs. (3.4)–(3.11). The basic condition at $r=0$ is that spacetime is nonsingular there. This is a consequence of the fact that we use polar slicing. Indeed, the lapse function with this choice of slicing decreases to zero when an apparent horizon is approached (should there be one in the spacetime). This implies (since singularities are avoided) that at the origin, we always have $g(r=0)=1$, and g, N, ϕ_1, ϕ_2 all have vanishing first spatial derivatives at

$r=0$. Indeed if we extend the range of r to include negative values, g, N, ϕ_1 , and ϕ_2 are symmetric about $r=0$ and their parities are conserved by the Eqs. (3.4)–(3.11). By their definitions, the quantities ψ_1, ψ_2, π_1 and π_2 are antisymmetric about $r=0$. They are zero at the origin and the antisymmetry allows us to determine ϕ_1 and ϕ_2 at the origin as first derivatives of ψ_1 and ψ_2 at $r=0$. The value of the lapse function is not prescribed at the origin but is determined by integrating the first-order equation (3.5) inward from the outer boundary.

At the outer boundary, we choose the lapse to be fixed at its initial value. We are free to choose the value of N at one point on each slice. The value of g at the outer boundary is not to be chosen but is determined by the evolution. It can be obtained either from Eq. (3.7) or from the Hamiltonian constraint equation (3.11). We choose to determine it using the latter equation, while we evolve g at any interior point using the former equation. The value of g at the boundary is related to an important parameter characterizing the system: the total gravitational mass (as measured at infinity) is

$$M = \frac{1}{2}r \left[1 - \frac{1}{g^2(\infty)} \right]. \quad (3.12)$$

The masses reported in this paper are obtained with this formula. As for the boundary conditions for the scalar fields, we place the outer boundary far enough out in the asymptotic region that we expect scalar waves to be only outgoing there. In the massless case the propagation speed is independent of the wavelength so the outgoing wave condition is simply given by $(1/N)(\partial\psi/\partial t) = (-1/g)(\partial\psi/\partial r)$. However, this condition is not usable for a massive field. We generalize this condition to include the effect of the mass on the dispersion relation to first order in m/ω . The dispersion relation for a massive Klein-Gordon field in the asymptotically flat region of the spacetime is given by $\alpha^2 k^2 = \omega^2 - N^2 m^2$, where $\alpha = N/g$ (the first spatial derivatives of the metric functions are of higher order in $1/r$). The condition which gives rise to this dispersion relation, when expanded to first order in m/ω , is

$$\ddot{\psi} = -\alpha\dot{\psi}' - \frac{N^2}{2}\psi. \quad (3.13)$$

In our present code this condition is implemented as our outer boundary condition for the scalar fields. However, since it is only for a first-order correction to the massless condition, it does not completely allow outgoing waves to escape the grid. We have observed partial reflection of waves in our calculations. In most cases the small amount of reflection has practically no effect on the accuracy of the calculations. However, in one particular case, namely, the migration of boson stars with lower masses from the unstable branch to the stable branch (to be discussed in Sec. IV C), the reflection is the major factor in limiting us from following the evolution for a longer time. We are currently working to improve this boundary condition for the scalar field.

F. Code tests

We have tested the modified MacCormack method described against the forward/backward MacCormack method, the Brailovskaya predictor corrector method, and the standard and extrapolated leapfrog method on wave equations in both Cartesian and spherical coordinates, and on a nonlinear partial differential equation which has many of the features of the Einstein equations we are solving, but with a known solution. We have found the modified MacCormack method outlined above superior to the others in maintaining accuracy, especially at late times in the evolution. The details of these comparisons will not be discussed in this paper.

Another important test is provided by evolving the equilibrium data, since in this case, we know what the result should be, namely, that the metric functions g and N should stay constant in time. This is not a trivial test since both ϕ_1 and ϕ_2 are evolving in time; only the correct nonlinear combination of their effects on the geometry is zero. Moreover, as we shall demonstrate in Sec. IV below, some of these equilibrium configurations are intrinsically unstable. We evolve these configurations without putting perturbations in; i.e., we let the equilibrium data be perturbed only by the inherent discretation error present in any numerical code. For a typical equilibrium star, e.g., one with $\phi(0)=0.40$ or $M=0.609$, we find that after a time greater than $t=100$, the maximum deviations of N and g from their equilibrium values are

less than 0.1% throughout the star. This is to be compared to the scalar fields' intrinsic oscillation period of 2π . The same star collapses with a dynamical time scale of $t \sim N/\dot{N} \sim 20$, when perturbed slightly (with a change in mass by less than 1%) by choosing $\delta\phi_1$ as described in Sec. III D. At $t=48$ the peak value of $g=10^2$ (compare to the peak value of $g=1.7$ at $t=0$) and the lapse at the center is $N^2=10^{-11}$ (compare to $N=0.75$ at $t=0$), indicating that a black hole has been formed. This evolution is shown in Figs. 9(a) and 9(b).

An important indicator of the accuracy and stability of the code is the deviation of the Hamiltonian constraint [Eq. (3.11)] from zero, which we closely monitor in all runs. In Fig. 1 a typical deviation of the constraint multiplied by r^2 is plotted against r for each instant of time for the dynamical evolution of a perturbed boson star (the evolution of this star is discussed in Sec. IV B). The factor r^2 is included so that it reflects the volume of space in which the error of the Hamiltonian constraint appears. The region where the error is largest is the region where most of the activity is going on. The spike at the boundary of the grid results from the use of a second-order derivative scheme near the boundary. Had we not multiplied the result by r^2 , the spike at large r at all times is less than 10^{-9} , and the error is the largest at the inner boundary $r=0$, where it is at most of order 10^{-6} at all times throughout the evolution. The data shown represent evolution up to $t=1500$. This is to be compared to the intrinsic oscillation period of 2π . We have

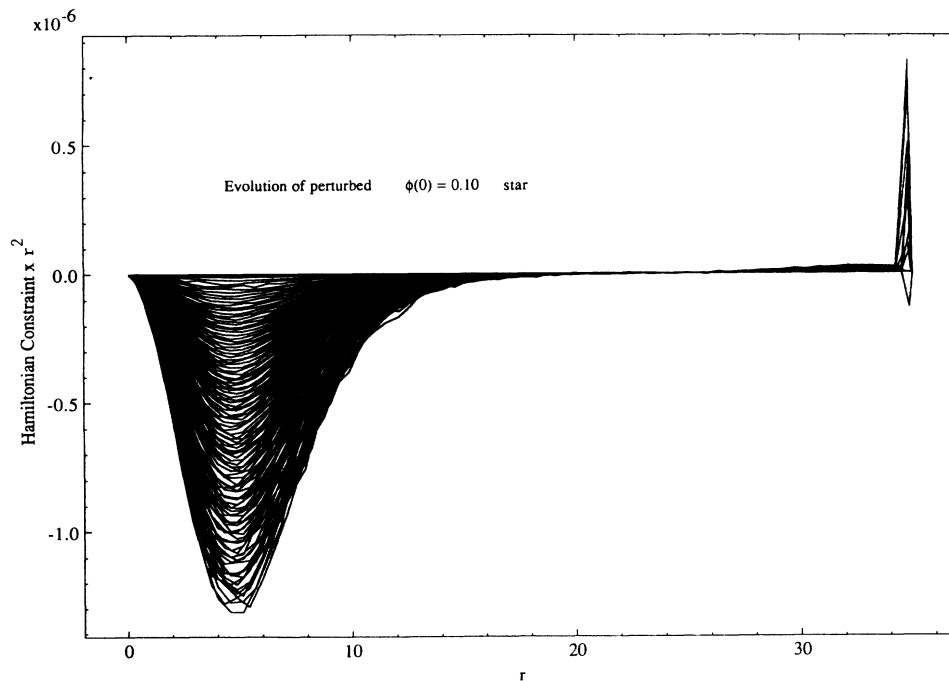


FIG. 1. The Hamiltonian constraint $G_{tt} - 8\pi GT_{tt} = 0$ [Eq. (3.11)] times r^2 is plotted against r at various times during the evolution of an oscillating boson star. (The evolution is studied in Sec. IV B.) The factor of r^2 reflects the volume of space in which the error in the Hamiltonian constraint appears. The spike at the outer edge of the grid appears because of a second-order boundary condition used there; without the r^2 factor this spike is only of order 10^{-9} . Without the r^2 factor, the error is largest at the origin, but does not exceed the 10^{-6} level there throughout the entire run, which lasts for $t=1500$, a time orders of magnitude longer than the intrinsic oscillation time scale (2π) of the scalar field.

terminated the calculation at this point only because of the computation time involved. Most of the results we report in the paper involve deviations of the Hamiltonian constraint by itself and multiplied by r^2 both less than 10^{-5} .

Another class of tests we have done is to compare the code to other codes we developed. We have mentioned the shift vector code which slices spacetime in a different manner. The two codes in all tests give physical quantities which agree with each other to high accuracy. We have further applied the code to weakly gravitating boson stars and compared the result to that of the Newtonian code based on Eqs. (2.17) and (2.18). The Newtonian system is much simpler mathematically, does not involve slicing and constraint problems, and some of the results can be obtained analytically. The relativistic code produces results agreeing with the Newtonian code for all cases studied. An example of the comparison is given in Fig. 6.

We have also performed tests to make sure that the results we obtained are not affected by parameters used in the numerical code (e.g., grid size, spatial extent of the grid, the order of derivative schemes, etc.). One such comparison between fourth- and sixth-order spatial derivative schemes with different size grids (i.e., the spatial extent of the grid) is shown in Fig. 10(b). We see that the results are independent of the parameters chosen.

We have performed single-time-step convergence tests which measure how well our spatial difference scheme is converging on a solution. If one assumes that the computed value of a particular quantity H differs from its true value H_0 by

$$H - H_0 = k (\Delta r)^\sigma, \quad (3.14)$$

where k is some constant and Δr is the grid spacing, then σ may be computed easily from

$$\sigma = 1 + \partial(\ln H') / \partial(\ln \Delta r), \quad (3.15)$$

where $H' \equiv \partial H / \partial(\Delta r)$. In practice, we have measured σ by computing the spatial integral of the Hamiltonian constraint over the star:

$$H = \int_0^{\text{surface}} (G_{tt} - 8\pi G T_{tt}) dr. \quad (3.16)$$

This quantity is computed using a fourth-order numerical integration scheme. In a typical case, we perturbed a $\phi(0)=0.40$ star by decreasing its central density by 10%. We then recompute the initial data as described in Sec. III D and evolve for one time step. Using four different grid spacings of $\Delta r=0.1$, $\Delta r=0.075$, $\Delta r=0.05$, and $\Delta r=0.025$, and choosing equal time steps for each grid spacing, we can compute several independent values of σ , which all lie in the range $3.1 < \sigma < 3.2$ for our fourth-order code. As one expects, the actual computed value of

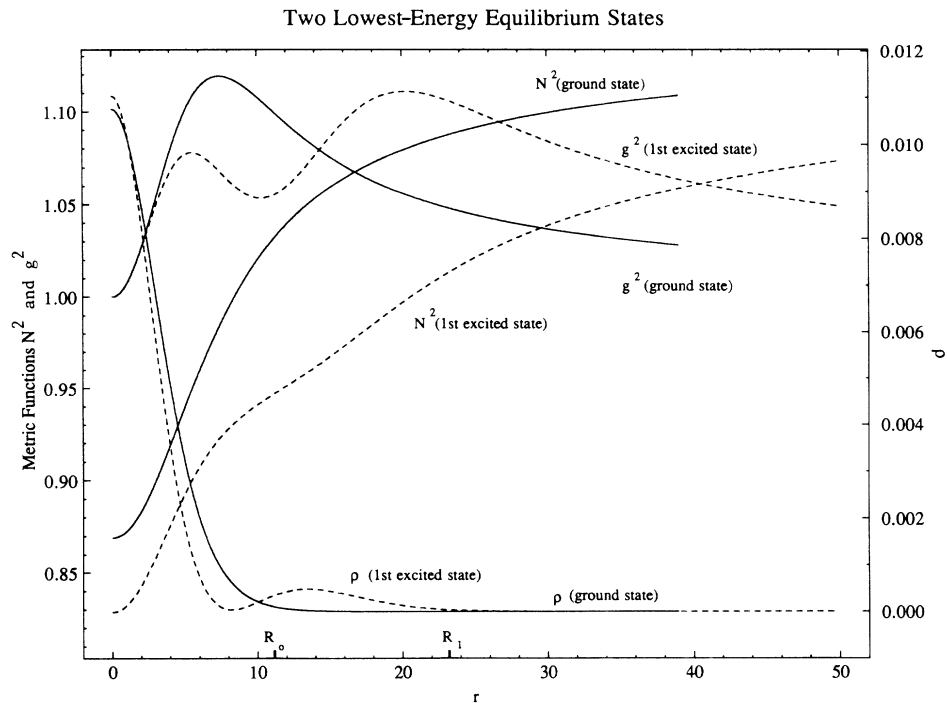


FIG. 2. The radial metric functions $N^2 = -g_{tt}$ and $g_{rr} = g^2$, and the energy density $\rho = -T'_t$ of the two lowest-energy equilibrium configurations are shown for the boson star with a central field value of $\phi=0.10$. The left vertical axis gives the value of the metric functions N^2 and g^2 , while the right vertical axis gives the value of the energy density ρ . The lapse N is not one at $r = \infty$, but is related to the equilibrium oscillation frequency ω_0 of the scalar field as measured by an observer at spatial infinity [$\omega_0 = m/N(\infty)$, where m is the mass of the scalar field]. The solid lines denote the ground state and the dashed lines denote the first excited state. The first excited state shows the shell-like structure which is a result of the node in the radial wave function ϕ . The points marked R_0 and R_1 denote the radii containing 95% of the mass of the ground-state and first-excited-state boson stars, respectively. Note that although the second peak of the first excited star is lower, there is much more mass in the “shell” due to the r^2 factor.

σ is found to be somewhat below the order of the spatial derivatives utilized in the scheme.

IV. EVOLUTION OF PERTURBED BOSON STARS

A. Equilibrium configurations

The equilibrium configurations of boson stars have been studied by many authors.^{5–12} In this subsection we give a brief description of these configurations to set the stage for the perturbation analyses.

A boson star is said to be in its n th excited state when the scalar field has n nodes in the radial direction. For a given total mass of the star, the one with no nodes has the lowest energy. In Fig. 2 the scalar field energy density is plotted against the radius r for a typical ground state (solid line) and a first excited state (dashed line). As in all other figures in this section, the quantities plotted are the rescaled dimensionless quantities given in Eq. (3.4). The scalar field $\phi(r)$ of the first excited state has a node at the circumferential radius $r \sim 7.8$. Also plotted are the structures of the gravitational field of the two configurations (solid lines for ground state, dashed line for first excited state) are shown. The left vertical scale is for the lapse and the radial metric coefficient g^2 . The fact that $g=1$ at $r=0$ is required by the regularity of spacetime near the origin (elementary flatness). That $g \rightarrow 1$ at large r is required by asymptotic flatness. The value of g^2 at large r is determined by the total mass of the star through Eq. (3.12). The lapse N is free for us to choose at one spatial point on each time slice. The natural choice is $N=1$ at $r = \infty$. But with our choice of t rescaled by Eq. (3.4), the lapse N is not one at $r = \infty$, rather, the value of $N(\infty)$ gives the equilibrium oscillation frequency ω_0 of the scalar field as measured by an observer at spatial infinity [$\omega_0 = m/N(\infty)$, where m is the mass of the scalar field]. In Fig. 2, R_0 (R_1) is the radius of the ground-state (first-excited-state) boson star, which is defined to be the radius containing 95% of the total mass M of the star, as read out from the form of g^2 (see Ref. 13).

Note that the Newtonian potential V is given by

$$V = \frac{1}{2} \left[\frac{N^2(r)}{N^2(\infty)} - 1 \right] \quad (4.1)$$

and the radii R_0 and R_1 give roughly the size of the gravitational potential well in Newtonian language. Figure 2 also shows the energy density $\rho = T_{\hat{t}\hat{t}}$ distributions of the two configurations as measured by observers at fixed circumferential radius r . We see that while the ground-state distribution (solid line) is qualitatively the same as an ordinary star, the distribution of that of the first excited state (dashed line) has a shell-like structure. In the next paper in this series, we shall show that this shell-like structure is unstable. Upon perturbation, it will collapse to a ground-state configuration. We focus on the behavior of the ground-state boson star in this paper.

The similarity of the ground-state boson star to a neutron star is evident in Figs. 3(a) and 3(b). Figure 3(a) gives the total mass M [determined by Eq. (3.12)] of the star versus the value of the scalar field ϕ at $r=0$. Similar

figures have been obtained by many authors.^{5–7} Figure 3(b) gives M vs R , the radius containing 95% of mass of the star. The inset, with a different ratio of horizontal to vertical scale, is the enlargement of the snail-like structure at small radius. We see that there is a minimum radius for equilibrium configurations, $R=2.79$ (remember R is the 95% mass radius). From Figs. 3(a) and 3(b), we

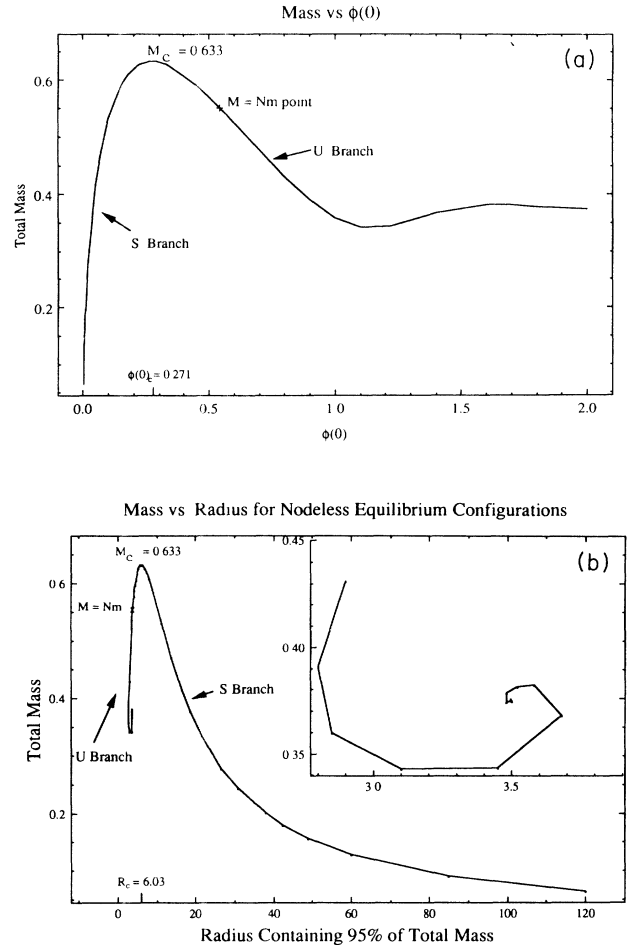


FIG. 3. (a) The total mass M (in units M_{Planck}^2/m) of the ground-state boson stars is plotted as a function of the central value of the complex magnitude of the scalar field $\phi(0)$. The maximum mass M_c occurs at $\phi(0)=0.271$. The point on the curve marked by a plus sign denotes the transition between configurations with positive binding energy to those with negative binding energy, which occurs at $\phi(0)=0.54$. Configurations on the S branch, to the left of the maximum, are stable with respect to infinitesimal perturbations, while those on the U branch are unstable. There are additional peaks at the large $\phi(0)$ end of the U branch. (b) The total mass M of the ground-state equilibrium configurations is graphed against the radius containing 95% of the mass, showing the similarity of boson stars to neutron stars. The inset in the upper right section of the figure shows an expanded view of the snail-like feature at the bottom of the U branch, or unstable branch. The S branch, or stable branch, is to the right of the peak of the curve. The transition point from positive to negative binding energy is marked by an \times on the U branch. The critical 95% radius, $R_c=6.03$, is also marked.

see that there is also a maximum mass: $M_c = 0.633 = 1.7 \times 10^{11}$ g (for a scalar field mass m of 1 GeV). We call the branch to the right of the peak in Fig. 3(b) the S branch [corresponding to the branch to the left of the peak in Fig. 3(a)] and the branch to the left of the peak the U branch [the branch to the right of the peak in Fig. 3(a)]. From Fig. 3(b) we see that the mass of the U -branch stars has a lower bound of $M=0.34$. The U branch includes the configurations in the snail-like structure (shown in detail in the inset). We shall see that these configurations, when perturbed, evolve in qualitatively the same manner as other configurations in the branch. We shall also see that the configurations in the U branch with mass $M < Nm$ [points above the $M = Nm$ point in Figs. 3(a) and 3(b)], although having positive binding energy such as those configurations on the S branch, have the same qualitative behavior under perturbation as the $M > Nm$ configurations (which we have studied) in the rest of the U branch. This result, that the qualitative evolution of boson stars is independent of whether the configurations have positive or negative binding energy, might be *a priori* unexpected.

We note that in Fig. 3(b), although the choice of parametrizing a configuration with a radius containing 95% of the mass might seem arbitrary, it is a useful parametrization because (i) the qualitative behavior of both the equilibrium lines and the behavior of evolution after perturbation will be the same if we use other definitions of the radius,¹³ and (ii) that during dynamical evolution, the value of ϕ at $r=0$ [the parameter used in Fig. 3(a)] is no longer a good characterization of the structure of the

whole star. On the other hand, the radius of the star is still useful in intuitive understanding of the evolution.

The S -branch and the U -branch equilibrium configurations are separated by the configuration with $dM/d\phi(0)=0$, which has been shown^{11,12} to be the transition point between stability and instability under infinitesimal perturbations which hold fixed the total mass and total number of particles. We shall study how the transition point is affected when more general kinds of perturbations are considered.

B. Perturbations of the S -branch stars

1. Relativistic analyses

The evolution of boson stars on the S branch after perturbations follows one single pattern, essentially independent of the location on the branch and types of perturbation considered. There are two broad types of perturbations as discussed in Sec. III D. Perturbations with both positive and negative values of $\delta\phi_{\max}/|\phi_{\max}|$ ranging from less than 1% to greater than 1 have been studied (where the subscripts “max” denote maximum value in the corresponding spatial distributions). For small perturbations, the perturbed star always oscillates with a dominant frequency, radiates some of the scalar field away to spatial infinity, and gradually settles down to another S -branch configuration with a total mass less than the perturbed value. (It is, of course, possible to, for example, increase the density in a region of the star so much that the star collapses; see, for example, a case studied in Sec. IV D. We exclude perturbation of this sort in this section.) In Fig. 4, a typical, but strong, initial perturbation

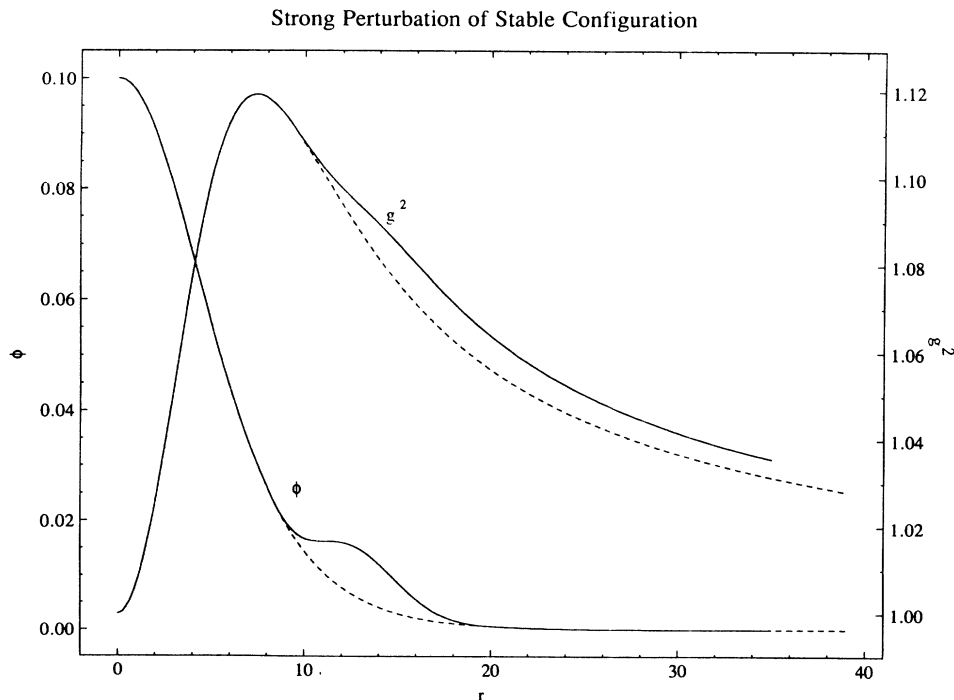


FIG. 4. A strongly perturbed S -branch boson star with $M=0.533$ [$\phi(0)=0.10$] is contrasted with the unperturbed configuration. The solid lines show the perturbed configuration, while the dashed lines show the unperturbed star. The left vertical axis shows the scalar field ϕ at $t=0$ (which is chosen to be real), while the right vertical axis shows the radial metric function $g_{rr} = g^2$. This perturbation mimics the effect of accretion of additional scalar field particles, as can be seen by the bump in ϕ between $r=10$ and $r=20$.

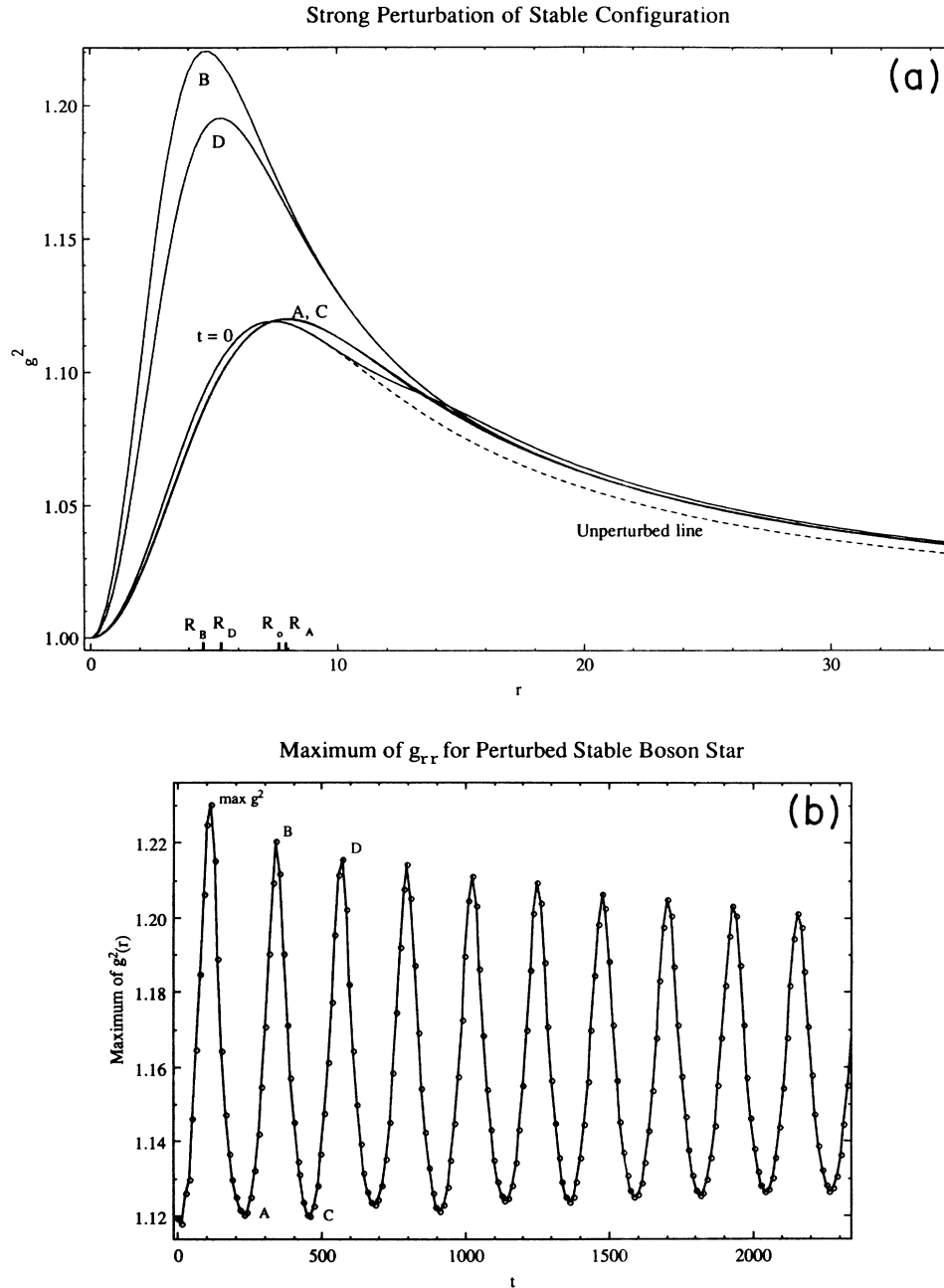


FIG. 5. (a) The evolution of the radial metric function $g_{rr} = g^2$ for the perturbed configuration given in Fig. 4 is shown. The initial perturbed configuration is labeled by $t=0$, which is contrasted with the unperturbed configuration denoted by a dashed line. The spatial distribution of g_{rr} is shown at later times marked A , B , C , and D , corresponding to coordinate times $t=226$, 339 , 458 , and 571 , respectively. The lines marked A and C are so close that they nearly overlap in this diagram. The positions of the peaks of these lines are marked by R_0 , R_A , R_B , and R_D . In this case $R_C = R_A$. The first minimum of the peak in g_{rr} is labeled by A , the subsequent maximum by B , the next minimum labeled C , and next maximum labeled by D . (b) The peak value of the radial metric function g_{rr} is graphed against time for the perturbed star shown in (a) for a much longer time. Each point in this figure corresponds to one curve in (a). The points labeled A , B , C , and D correspond to those labels in (a). The oscillations are clearly decaying as the evolution proceeds, although the decay rate is decreasing. (c) The radial position of the peak of g_{rr} is shown as a function of time for the evolution depicted in (b). The points labeled A , B , C , and D correspond to the same labels in (b). The discrete nature of the curve is an artifact of the printing resolution used in dumping the data during the computer run; the actual grid resolution of the run was much finer. Again, the oscillations are clearly decaying. Note that when the core of the star reaches its maximum size during an oscillation, the peak of g_{rr} is a minimum, and when the core reaches its minimum size during an oscillation, the peak of g_{rr} is a maximum. (d) The total mass M of the star shown in (a)–(c) is shown as a function of time. The mass is measured by the asymptotic value of the radial metric function g_{rr} . The points labeled A and C denote the first two points of maximum expansion, which are similarly labeled in (a)–(c). After an initial sharp burst of scalar radiation, there are subsequent smaller bursts at each maximum expansion. The decay in the radiation rate is clearly seen.

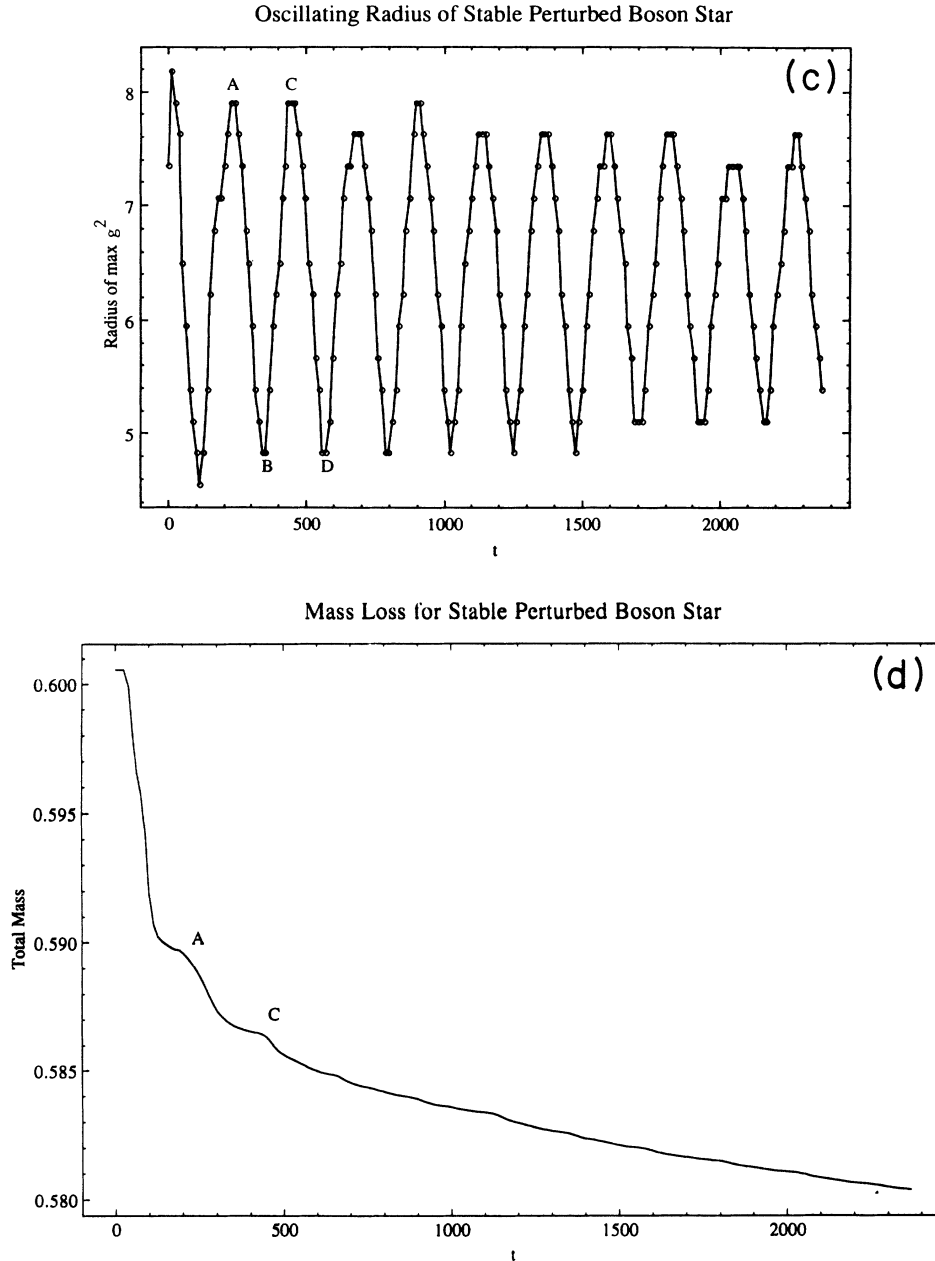


FIG. 5. (Continued).

of the second type used in the study is shown. In this example we have chosen a strong perturbation so that the interesting features of the evolution will stand out. The dashed lines are the equilibrium configuration (the left vertical scale refers to the scalar field ϕ and the right vertical scale refers to g^2) whereas the solid lines give the initial values for evolution. This perturbation mimics the effect of additional scalar particles being accreted by the boson star.

The subsequent evolution of the star is shown in Figs. 5(a)–5(d). Figure 5(a) shows $g^2(r)$ for various times. The A , B , C , D lines correspond to, respectively, $t=226,339,458,571$. The positions of the various peaks of the curves are given, respectively, as $R_{A,B,C,D}$, where the peak for the unperturbed equilibrium configuration

(dashed line) is denoted as R_0 (in this case, $R_C=R_A$). It is clear that the star is oscillating about an equilibrium configuration close to but more compact than the original unperturbed configuration, and is slowly converging towards it. These oscillations are shown for a longer time in Fig. 5(b). The maximum of the spatial distribution of $g^2(r)$ at an instance of time is plotted against time. The radius of the star versus time is also shown in Fig. 5(c). The points A , B , C , and D correspond to the lines shown in Fig. 5(a). We see that these oscillations are indeed slowly decaying.

In Fig. 5(d) we have plotted the total mass of the system, determined by reading the asymptotic value of the metric coefficient g_{rr} [see Eq. (3.12)]. The system is clearly losing mass as it evolves. In fact, one can see clearly

that the first few outward oscillations produce bursts of scalar radiation, and the points labeled *A* and *C* correspond to the similarly labeled peaks in Figs. 5(a) and 5(b). This effect continues throughout the evolution, although as the oscillations die down, less and less matter is emitted through successive oscillations. This radiation damping mechanism is a generic feature of the oscillating boson star, and will be discussed further in later sections of this paper. The oscillation frequency in terms of proper time at infinity can be easily read out from Fig. 5(b) to be $f = 1/[228N(\infty)] = 4.17 \times 10^{-3}$, which is constant in time to high accuracy. The decay rate Γ is an increasing function of the oscillation amplitude. For the amplitude of the case shown in Figs. 5, $\Gamma = 2.8 \times 10^{-3}$ [amplitude damped to half in the time $1/\Gamma$ (proper time at infinity) if the same rate is kept]. For comparison, the same initial star perturbed with a much smaller amplitude showed a damping rate Γ of order 10^{-6} .

In Fig. 6 we plot the oscillation frequency versus mass of the case just discussed together with those of the other slightly perturbed *S*-branch star (so that the masses of the

perturbed configurations are within 0.1% of the unperturbed equilibrium configurations, i.e., $\delta M/M \leq 10^{-3}$). These frequencies are shown as squares lying on the solid line. They are the fundamental oscillation frequencies of the *S*-branch stars.

Note that the oscillation frequency marked by the solid line steadily increases as one moves from very dilute, low mass stars (softer stars) to more compact and massive stars (stiffer stars) in the regime below the critical mass $M_c = 0.633$. There is a turnaround near M_c ; the oscillation frequency has a sharp decline, signaling the onset of the instability of the fundamental mode with ω^2 approaching zero. Beyond M_c , the oscillation frequency ω has a positive imaginary part. We will return to this point in Sec. IV C, where we discuss the unstable branch.

If an *S*-branch star is perturbed significantly, it oscillates with a frequency below the solid line in Fig. 6, independent of whether the perturbation is one that increases or decreases the mass. These perturbed configurations radiate the scalar field to infinity, lose mass, move horizontally in Fig. 6, and slowly return to

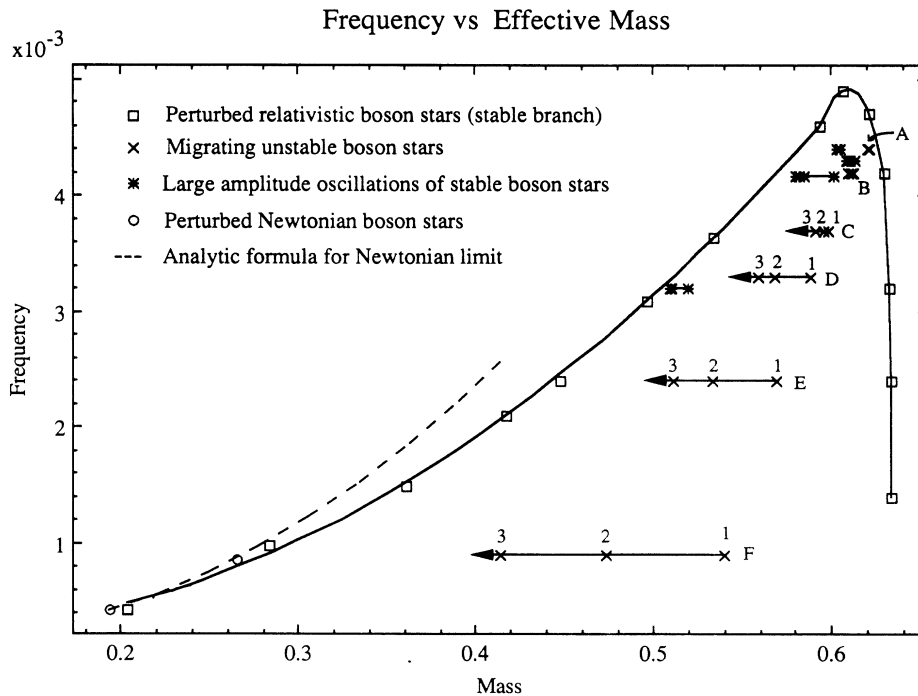


FIG. 6. The oscillation frequencies of various boson stars are plotted against their mass. The squares, connected by the solid curve, are obtained by slightly perturbing stable (*S*-branch) boson stars. The curve reaches a peak value near $M=0.587$ and then the right branch of this curve approaches zero as the critical mass is approached. The asterisks are obtained by strongly perturbing *S*-branch stars. These stars start out oscillating with a frequency below the solid line. As they evolve and radiate mass away, they move horizontally towards the solid line. The open circles are obtained by perturbing low mass, Newtonian boson stars and evolving them with the Poisson-Schrödinger equations. The \times 's are obtained by perturbing boson stars on the *U* branch. Six *U*-branch stars labeled *A*–*F*, are shown migrating to the *S* branch, as indicated by the arrows. These stars have initial, unperturbed masses of 0.632, 0.620, 0.609, 0.598, 0.579, and 0.548, respectively. In this figure, they move to the left, toward stars with masses of 0.58, 0.56, 0.54, 0.51, 0.45, and 0.3, respectively. The crosses marked along each track represent equal time intervals, and are labeled numerically in increasing order of time. The track labeled *A* has three unlabeled crosses, barely resolvable on this scale. The track labeled *F* here has a mass 0.548, which is below the $M = Nm$ point. Hence although it is a configuration with excess energy initially, it manages to radiate away the excess mass and migrates to the *S* branch, with a much lower mass. Finally, the dashed line is obtained from the analytic formula Eq. (4.3). The excellent agreement of both the relativistic and Newtonian calculations to the analytic formula is evident. For a full discussion of these points, see the text in Sec. IV.

the solid line. This process is a very generic feature of perturbed boson stars. Some examples of this behavior that we have studied in our simulations are shown in Fig. 6 marked with an asterisk.

An expanded diagram showing the evolution of these strongly perturbed stars is given in Fig. 7. The A marked with an asterisk is obtained by subtracting scalar particles from an $M=0.533$ star [corresponding to $\phi(0)=0.1$] on the S branch. The perturbed initial mass is $M=0.519$. It oscillates with the frequency 3.2×10^{-3} , whereas the B marked with an asterisk is obtained by adding scalar particles to the same star, so that the perturbed initial mass is $M=0.601$. In fact, this is the star shown in Figs. 4 and 5. The oscillation frequency is 4.17×10^{-3} .

The star at point C is again the result of perturbing a $\phi(0)=0.1$ star, but this time it has been perturbed by adding kinetic energy through a perturbation in $\dot{\phi}_1$ (cf. Sec. III D). In this case, the perturbed initial mass is $M=0.612$, and as it radiates away some of its mass it moves to the left in the frequency versus mass diagram. Finally, the star at point D is the result of perturbing a boson star with an initial mass of $M=0.632$. Note that this initial star lies on the right-hand slope of the frequency versus mass curve. We have perturbed this star by decreasing its central field by 25%, corresponding to a perturbed mass of $M=0.604$. As in the other cases, this boson star heads toward the left-hand slope of the frequency versus mass curve as it radiates scalar field particles to infinity.

The frequency versus mass diagram is particularly useful in that it enables us to determine the final point of

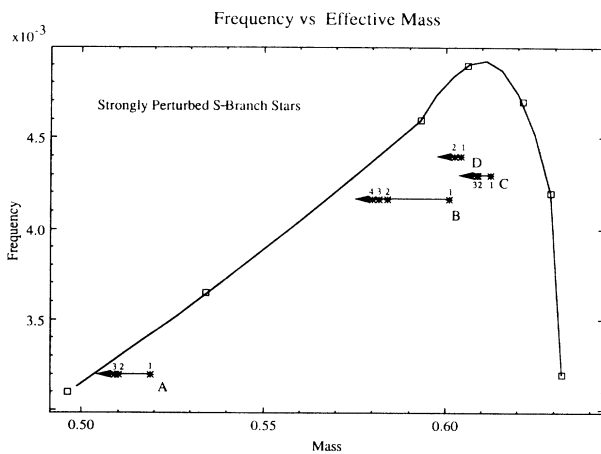


FIG. 7. An expanded view of Fig. 6 is given, showing only the strongly perturbed S -branch stars, labeled A , B , C , and D , and the fundamental oscillation frequencies of the S branch (solid line). The tracks marked A , B , C , and D are obtained by perturbing S -branch stars with initial masses of $M_0=0.533$, $M_0=0.601$, $M_0=0.612$, and $M_0=0.632$, so that stars from both sides of the S -branch frequency curve are represented. The asterisks along each track representing equal time intervals are labeled in increasing order of time evolution, indicating the decreases in the mass of the stars due to scalar radiation to infinity. The decay rate is clearly decreasing with the asterisks corresponding to later time clustering up. For details of the specific perturbations used, see the text in Sec. IV B 1.

evolution of a perturbed S branch star. (We shall see that it also enables us to determine the final point of evolution of U -branch star resulting from a certain type of perturbation in Sec. IV C.) From Fig. 7 we see that the initial configuration A will end up with a mass about $M_A=0.505$, while configurations B , C , and D will end up with masses of $M_B=0.565$, $M_C=0.575$, and $M_D=0.580$, respectively. The time scales involved for the evolution shown on the diagram are typically on the center of $t=500$ to 2500. Since the decay time is so long, the stars will not settle down at their new equilibrium positions for at least another order of magnitude in time or more. The data points marked with an asterisk (labeled by 1,2,3,4) represent equal intervals of time evolution. Some asterisks representing later times are barely resolvable, showing clearly that the rate of scalar field emission is decreasing rapidly as the oscillation damp out; i.e., the decay rate Γ decreases as oscillation amplitude decreases. We provide an understanding of this phenomenon in the next subsection.

This damping of oscillations through radiating scalar field to infinity is crucial in many ways to the understanding of the evolution and formation of the boson star. In the following subsection we will analyze these oscillations and damping in the Newtonian limit. The Newtonian analysis has the advantage that it is free of complications coming from the choice of slicing and violation of the constraint equation.

2. Newtonian analysis

In Sec. III we have shown that the relativistic system reduces to a Schrödinger equation with $\hbar=1$ coupled to a Newtonian gravitational potential. The Schrödinger field $\tilde{\phi}$ is bounded by the Newtonian potential well generated by the star itself. The equilibrium configurations (Newtonian boson stars) are obtained by substituting $\tilde{\phi}=\tilde{\phi}_0(r)e^{-i\tilde{\omega}_0 t}$, and $V(r,t)=V(r)$ into (2.17) and (2.18). These then become an eigenvalue problem with eigenvalue $\tilde{\omega}_0$. A typical Newtonian boson star with total mass $M=0.206$ is shown in Fig. 8. The left vertical scale is the magnitude of the Schrödinger field $\tilde{\phi}_0(r)$ rescaled by $\sqrt{4\pi G}$. The right vertical scale is the Newtonian potential $V(r)$. We perturb the Newtonian boson stars by changing the distribution to $\tilde{\phi}(r,t)=\tilde{\phi}_0(r)e^{-i\tilde{\omega}_0 t}+\delta\tilde{\phi}(r,t)$. (Only perturbations of the second type (cf. Sec. III D) are possible in the Newtonian case since the Schrödinger equation [Eq. (2.17)], is first order in the time derivatives.) The subsequent evolution for perturbed Newtonian boson stars is the same as for the low mass relativistic boson stars on the S branch. [For example, for $M \sim 0.3$, the radius $R=35.1 \approx 50(2M)$. Hence the Newtonian approximation is accurate for M smaller than that.] The oscillation frequencies of the perturbed configurations versus mass of the Newtonian stars are shown in Fig. 6 as circles. These were computed by evolving numerically the Newton-Schrödinger system [Eqs. (2.17) and (2.18)]. With the simple Newton-Schrödinger system, these oscillations of the Newtonian star can easily be understood. The perturbation $\delta\tilde{\phi}$ is approximately evolving in the po-

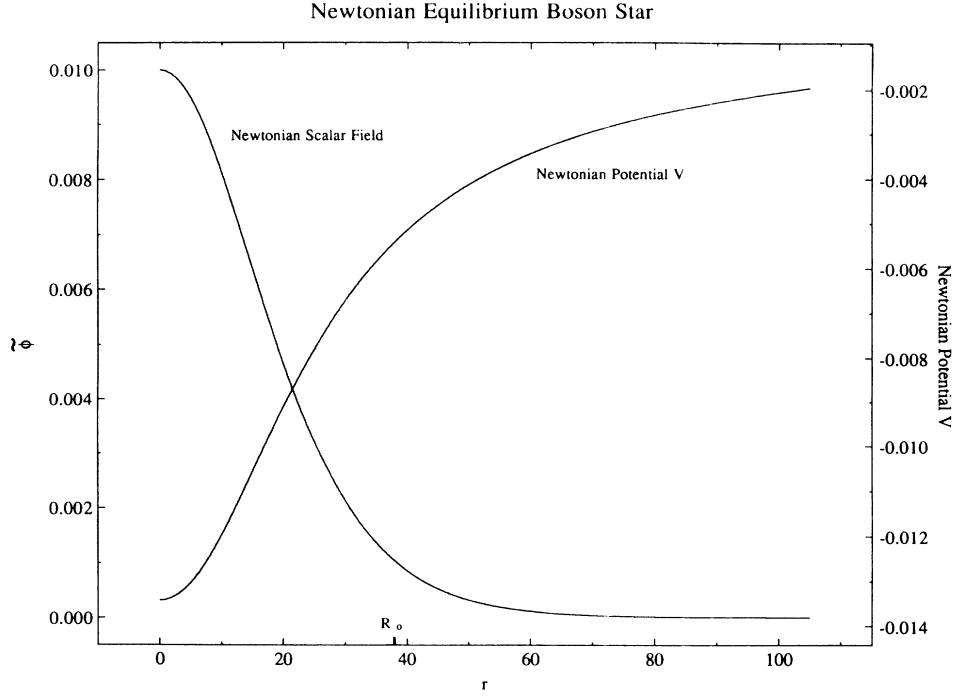


FIG. 8. A typical Newtonian boson star with a mass $M=0.206$ is shown, along with the Newtonian potential generated by the star. The magnitude of the central scalar field of this star is $\tilde{\phi}(0)=0.01$. The left vertical scale shows the value of the Schrödinger field and the right vertical scale shows the value of the Newtonian potential V . The point labeled R_0 gives the radius containing 95% of the total mass of the star, and is taken as the size of the Newtonian potential well created by the star.

tential well generated by the unperturbed configuration $\tilde{\phi}_0(r)$. The fundamental oscillation of $\delta\tilde{\phi}$ has a wavelength

$$\lambda \approx 2R_0, \quad (4.2)$$

where R_0 is the radius of the potential well (the radius of the equilibrium star). The angular frequency of the oscillation of $\delta\tilde{\phi}$ is

$$\tilde{\omega} \approx \frac{1}{2m} \left[\frac{2\pi}{\lambda} \right]^2 + mV_0 \approx \frac{1}{2m} \frac{\pi^2}{R_0^2} - m \frac{GM}{R_0}, \quad (4.3)$$

where the potential well is approximated by a step potential. (The potential of the Schrödinger equation in fact also contains in the gravitational potential due to $\delta\tilde{\phi}$ coupled with $\tilde{\phi}_0$. This term is linear in $\delta\tilde{\phi}$. It gives rise to a modulation of the oscillations of $\delta\tilde{\phi}$.) The frequency ($\tilde{\omega}/2\pi$) given by Eq. (4.3) is plotted against mass in Fig. 6 as the dashed line. Note the excellent agreement with the numerical data of the Newtonian stars and the lower-mass relativistic stars.

As discussed in the previous section, the oscillations are slowly damped as scalar radiation is emitted. The damping of the oscillations in the Newtonian case can be understood easily.

The perturbation $\delta\tilde{\phi}$ is approximately evolving in a fixed potential V_0 generated by the equilibrium $\tilde{\phi}_0$. If V_0 were exactly the potential the field evolves in, the state with $\tilde{\omega}$ given by Eq. (4.3) is a negative-energy state and no radiation to infinity is possible. There is, however, in addition to V_0 , a time-dependent part of the potential which is generated by $\delta\tilde{\phi}$ itself. The potential is time

dependent since the field is no longer a solution to the eigenvalue equation with $\delta\tilde{\phi}$ nonzero. This time-dependent perturbation to the potential is driving a transition of the field into positive-energy states, and in turn, leads to scalar radiation to infinity. The damping mechanism is highly nonlinear and the damping rate is of high power in $\delta\tilde{\phi}$, leading to a small damping rate in all cases studied.

The Newtonian analysis developed in Sec. III and used in this subsection is particularly useful in studying the initial stage of the formation of a boson star. A detailed study of this process will be reported in a future publication.

C. Perturbations of the U -branch stars

In this subsection we show (i) that the U -branch stars are unstable to *arbitrary* kinds of perturbations and (ii) what evolutionary paths these various perturbations of the U -branch stars lead to. Point (i) is a confirmation of previous result^{11,12} (now obtained under generic perturbation). Point (ii) turns out to have important implications on the formation of a boson star, as we shall see immediately.

In general, if the density of a star on the U branch is increased, a gravitational collapse will be initiated and the evolution will lead to a black hole, with a mass essentially the same as the initial perturbed configuration. Only a minimal amount of scalar radiation is emitted to infinity in the process. For typical cases we find that the mass of the radiated scalar field is well under 0.1% of the mass of the perturbed U -branch star. This result is essentially independent of whether we increase the density of the star by a first- or second-type perturbation (cf. Sec.

III D), although exceptions can easily be arranged: We can put in scalar field in the form of outgoing radiation in the outer part of the star. The star will still collapse to form a black hole but the amount of scalar radiation is

essentially the arbitrary amount that we put in initially.

A typical collapse is shown in Figs. 9(a) and 9(b). We slightly increase the central density of an $M=0.609$ U -branch star so that the perturbed configuration has the

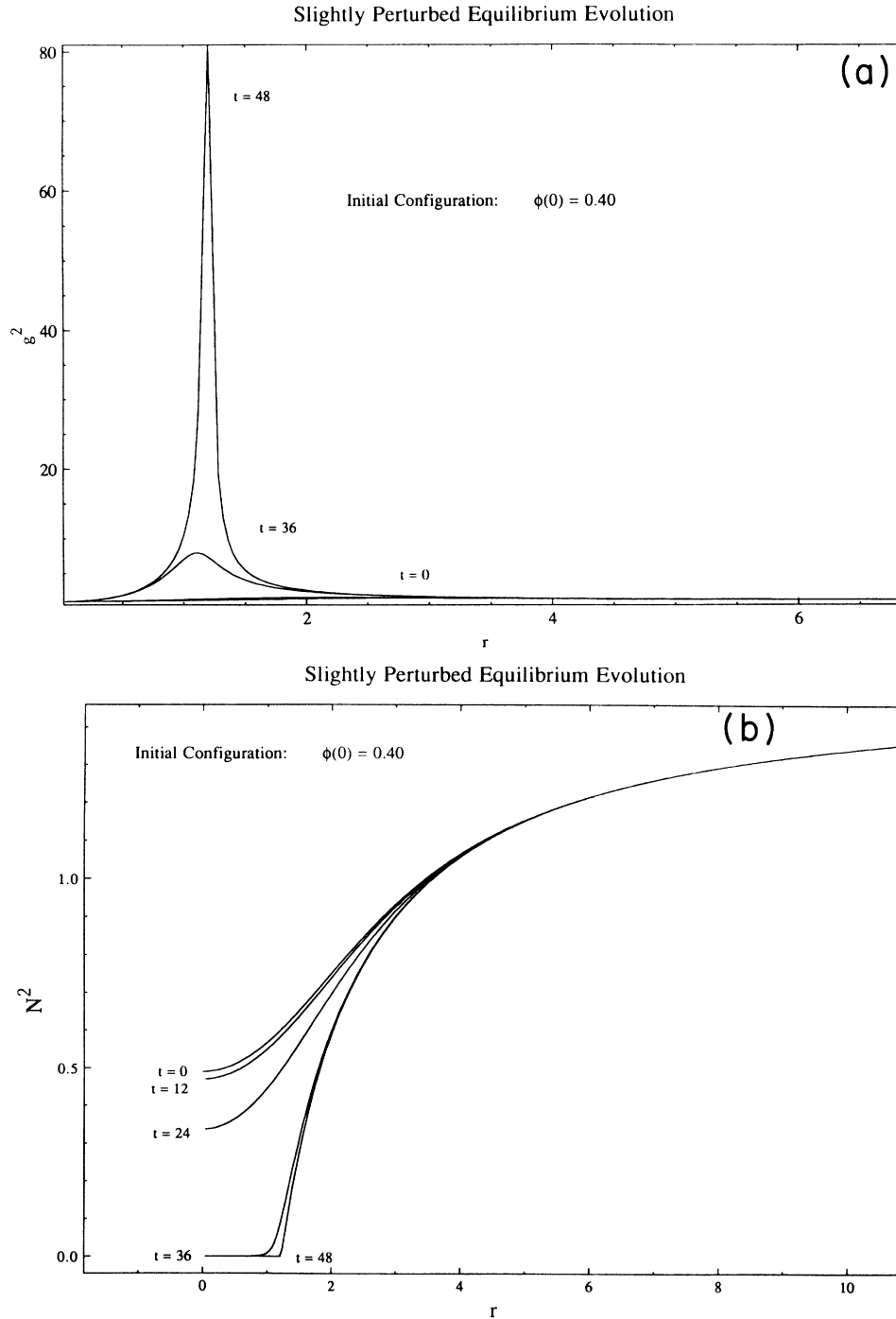


FIG. 9. (a) The evolution of the radial metric function $g_{rr} = g^2$ of the slightly perturbed boson star from the U (unstable) branch is shown for a perturbation which slightly increases the central scalar field. The unperturbed configuration had a mass of $M=0.609$ [$\phi(0)=0.40$]. The star rapidly collapses to a black hole. The initial, perturbed configuration is labeled $t=0$, and two later times are labeled $t=36$ and $t=48$. The rapid growth of the metric function g_{rr} is indicative of the formation of a strong field configuration. Because of the use of polar slicing, which dips to the “past,” the peak is not located at $r=0$. (b) The evolution of the metric function $N^2 = -g_{tt}$ is shown for the same star presented in (a). Various time slices are labeled by coordinate times $t=0, 12, 24, 36,$ and 48 , showing clearly the formation of a black hole. The lapse function collapses as the apparent horizon is approached. By $t=48$, N^2 is down to 10^{-11} .

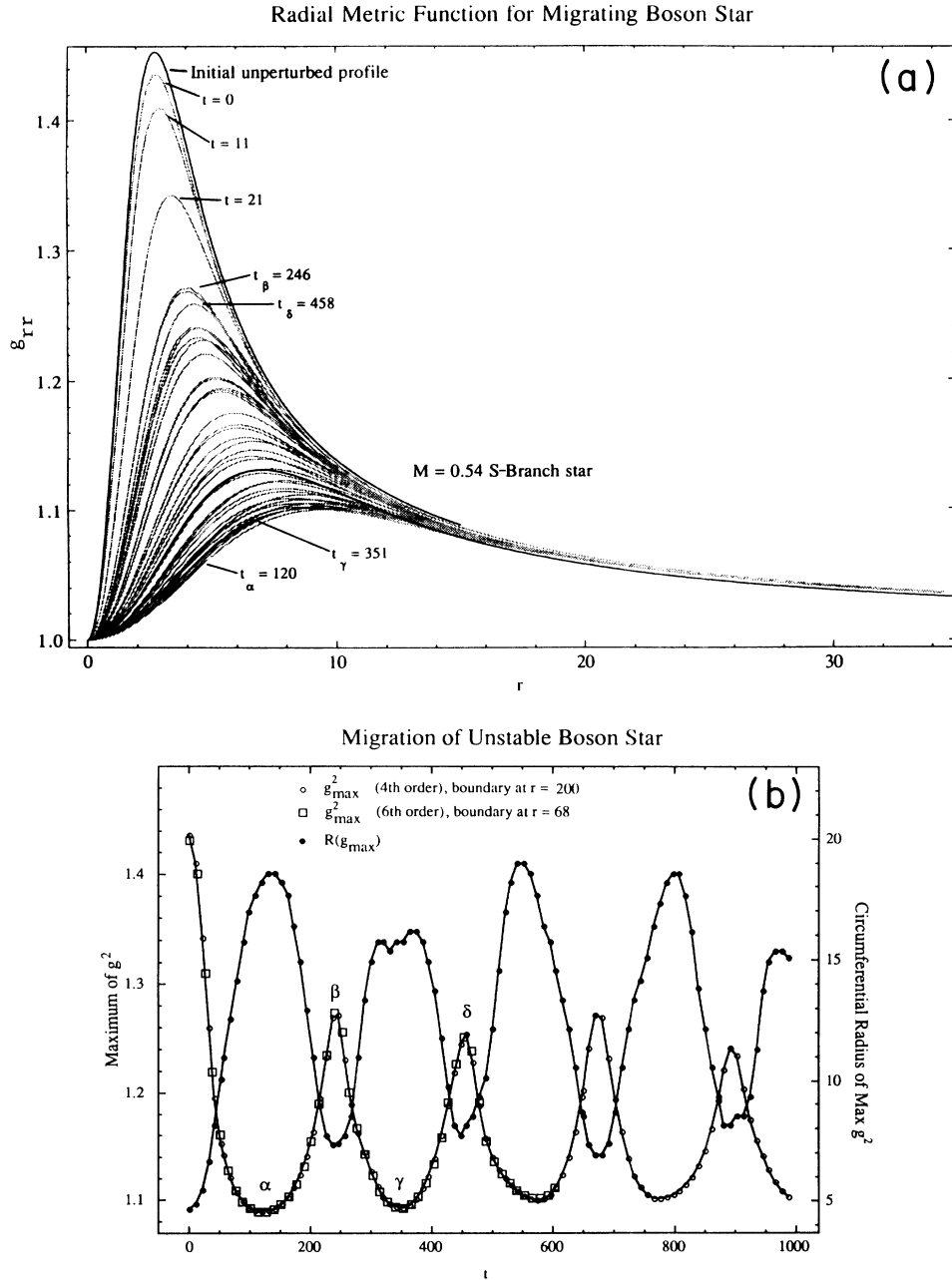


FIG. 10. (a) The radial metric function $g^2 = g_{rr}$ is shown at various times for a boson star migrating from the U branch to the S branch. The unperturbed star, shown with a dark line, is the same as that shown in Figs. 9(a) and 9(b). But here we have decreased the central density by 10%, with the resulting profile, shown as a lighter line, labeled $t=0$. Subsequent evolution is shown as light lines, with some times highlighted with labels. At times $t=11$ and $t=21$, note the rapid drop in the peak of g_{rr} as the star initially expands. The times labeled t_α and t_γ correspond to the first two minima in the peak of g_{rr} , which occur when the core of the star reaches its local maximum size, while the times labeled t_β and t_δ correspond to the first two maxima in the peak of g_{rr} , which occur when the core of the star reaches its local minimum size. For comparison, the equilibrium profile of an $M=0.54$ S -branch star is shown as a dark line. The migrating star is oscillating about an S -branch star with a mass near this one (in the asymptotic region g^2 is not oscillating but instead monotonically decreasing in time due to the mass loss). This mass is consistent with the mass determined from the frequency vs mass curve shown in Fig. 6. (b) The oscillations of the migrating boson star shown in (a) are shown for a longer time. Each point in this figure corresponds to a curve in (a). The points marked α , β , γ , and δ correspond to the same times labeled in that figure. The left vertical axis shows the value of the maximum of the radial metric function $g^2 = g_{rr}$ at a given time, while the right vertical axis shows the spatial position of this peak. The open circles are obtained using our fourth-order code, with the outer boundary of the computer grid placed at $r=200$, while the open boxes are obtained using our sixth-order code, with the outer boundary placed at $r=68$. The evolution for the two runs is indistinguishable as discussed in Sec. III F. The solid circles show the position of the peak of g_{rr} . During each outward oscillation of the core, the metric function g_{rr} decreases, and with each inward oscillation of the core it increases.

total mass $M=0.615$. The time development of $g^2(r)$ is shown in Fig. 9(a). The difference between the unperturbed radial metric function $g_0^2(r)$ and the initial perturbed $g^2(r)$, labeled as $t=0$, is very small and is not shown here. The corresponding lapse functions are shown in Fig. 9(b). We see that at late time the lapse has collapsed dramatically. [Remember that we use polar slicing, which decreases the lapse when the apparent horizon is approached (cf. Sec. III A).] In fact, by $t=48$, N^2 in the inner part of the star has dropped to about 10^{-11} . The radial function $g^2(r)$ at late time develops a sharp peak as the spatial slice dips back to the “past” (“past” in the sense of an ingoing Finkelstein coordinate). A black hole is formed. In fact, one may note from the position of the large gradient in N or the coincident peak in g that the radius of the black hole is $r=1.22$, or since the initial mass of the star is $M=0.615$, nearly all the matter has ended up inside the hole radius at this time.

In the mass versus radius diagram [Fig. 3(b)] this evolution is a horizontal line to the left of the U -branch line of equilibrium, plunging into the line $R=2M$. Stars throughout the U branch show the same behavior, independent of whether the star is on the snail-like structure [the inset in Fig. 3(b)], or above or below the $M=Nm$ point. We might expect that the star with excess energy ($M > Nm$) might radiate more scalar field to infinity. However, this turns out not to be the case.

If the density of a star in the U branch is decreased, no matter whether the decrease is in the central part of the star (so that gravitational attraction to the outer part is decreased) or it is in the outer part of the star (so that the pressure to the core of the star is decreased), the star explodes in radius, and moves to the right in the M - R diagram [Fig. 3(b)]. After it crosses the line of equilibrium S -branch configurations, part of the star falls back, while part of the outer region of the star escapes to infinity. The recontracted core of the star oscillates about an S -branch equilibrium configuration. *The U -branch star has migrated to the S branch.* The scalar radiation obtained is significantly more than in the collapse case. For the cases we have studied, we see that ranging from less than 1% to more than 20% of the mass of the original configuration is radiated in the initial burst, while subsequent oscillation sends out less radiation. In Fig. 10(a) the radial metric function $g^2(r)$ is shown at various times for a migrating, U -branch boson star with an unperturbed central density of $\phi(0)=0.40$. The initial configuration has its peak at $r=3.7$ with a peak value $g^2=1.45$. As the star expands, the peak slides down as the position of peak moves out. (The profile of g^2 at $t=11$ and $t=21$ are shown.) At $t=120$, denoted t_α in the figure, the expansion of the core halts and it begins to recontract. The peak of g^2 is located at $r=8.9$ and is substantially lower. The migrating star then settles down through a long period of slowly damped oscillations. The profiles of g^2 at some selected moments in this oscillation phase are shown. In particular, t_β is the time when the oscillating core reaches its first minimum radius. It then bounces back out until t_γ , then recontracts until t_δ . For comparison, the g^2 of an $M=0.54$ S -branch star, which the migrating star oscillates about is also shown. Note

that the asymptotic value of g^2 , which is tied to the total mass by Eq. (3.12), is not oscillating but is monotonically decreasing as scalar field is being radiated. In Fig. 10(b), these oscillations are shown for a long time. The left vertical scale is for the peak value of g^2 at different times, and the right vertical is the circumferential radius of these peaks. (This radius is somewhat less than the 95% radius in Sec. III, but is more convenient for this plot.) The point marked $\alpha, \beta, \gamma, \delta$ corresponds to $t_\alpha, t_\beta, t_\gamma, t_\delta$ in Fig. 10(b). These oscillations are of the same nature as those shown in Fig. 5(b) except that in the present case the oscillations have larger amplitudes initially. Hence when plotted in Fig. 6 (frequency versus mass) they fall below the dashed line (represented by crosses), as in the cases of strongly perturbed S -branch stars Fig. 7 discussed in Sec. IV B 1.

The six crosses shown in Fig. 6 correspond originally to U -branch stars with masses 0.632, 0.620, 0.609, 0.598, 0.579, 0.548 before the migration. In Fig. 6 we show a detail of these points labeled A through F , respectively. The data points labeled by 1–3 represent equal intervals of time evolution. As the oscillations decrease in amplitude due to the emission of scalar radiation, as discussed in the previous section, the decay rates decrease. In cases A , B , and C , the change in decay rate is not obvious. This is due to the fact that the boundary of the grid we have used is far out at large r . With the total mass of the configuration being read out at the boundary, it takes some time for the outgoing radiation to reach the boundary and for the mass contained within the boundary to decrease. In Fig. 6 we can obtain the mass they end up to have as S -branch stars. They move horizontally and hit the solid line at 0.58, 0.56, 0.54, 0.51, 0.45, and 0.3, respectively. These values are consistent with the masses determined by comparing oscillations of the star to an equilibrium configuration, as in Fig. 10(a).

We note that the U -branch star with $M=0.548$ is below the $M=Nm$ point in Fig. 3(b). Hence it is a configuration with excess energy (negative binding energy). The determination of the frequency of this star is less accurate, as its oscillation period is quite long, and we have evolved it only through one complete cycle. The long oscillation period of the lower-mass migrating stars, coupled with the spatial size of the S -branch stars to which they are migrating, makes these calculations very expensive in terms of computer time. We have performed calculations on the U -branch stars with masses down to 0.530, and in all cases, after significant expansion and initial mass loss, the inner core oscillates back inward; the stars manage to radiate the excess energy away as scalar radiation and settle down as S -branch stars, which always have positive binding energy. We note also that we have taken stars on the S branch and perturbed them in such a way as to increase their mass so that $M > Nm$, and these stars oscillate just as their positive binding energy counterparts. However, excess energy U -branch stars migrate to dilute S -branch stars, and we do not preclude the possibility that some will disperse entirely. These points have important implications on the formation of a boson star. This theme will be explored further in a future paper.

We have shown that a U -branch star will collapse or migrate to the S branch, depending on whether the perturbation increases or decreases the energy density of the star, but *independent* of whether the density is changed in the core or in the outer region of the star. However, the more generic perturbation would consist of a combination of the various perturbations considered above. For example, one might ask how an unstable boson star would evolve if the perturbation increases the density in part of the star while decreasing it in other parts. We have studied various perturbations of this sort. The outcome depends on the perturbation parameters chosen. We will not discuss each case in detail, but instead give the following generic results.

(i) The evolution always brings the star away from the U -branch configuration. The U -branch star is unstable under *any* kind of perturbation.

(ii) Increased density in the core with decreased density in our region can lead to either migration or collapse depending on the parameters chosen. The same behavior is seen if the perturbation decreases the density in the core and increases it in the outer region.

(iii) Once the core starts collapsing, if the central values of the scalar fields are rapidly increasing, the star

will not bounce back. (However, we have seen in a mixed perturbation that a mild initial inward oscillation may be followed by an expansion and migration.) Under rapid collapse, the runs we have done show that the core region monotonically approaches a black hole, whereas if the core is exploding initially, depending on the perturbation put on the shell, a later collapse is possible. Both expansion and collapse of the outer region are reversible.

One result we want to stress before we end this subsection is that, although exceptional cases can be arranged, the generic outcome of a perturbed U -branch boson star that initially expands is the oscillation about and the gradual settling down to a S -branch star, and this migration to the S branch is seen under very general types of perturbations.

D. Detailed study of the S - U transition point

It has been shown in Refs. 11 and 12, that for infinitesimal perturbations with fixed M and N , the transition between stability and instability occurs at the point of $\partial M/\partial\phi(0)=0=\partial M/\partial R$, i.e., the peak of the curve in Fig. 3(b). It corresponds to a configuration with $M=M_c=0.633$, $\phi(0)=\phi_c(0)=0.271$, and $R=R_c=6.03$. In this subsection, we study this transition point by following the dynamical evolution of the configurations lying close to it. The point we want to bring out in particular is that, while for perturbations with finite magnitudes, or perturbations which allow M and N to change, as we want to consider in general, there is no longer a notion of an exact transition point (indeed, for configurations close to the peak, one configuration can be regarded as a perturbation of another), nevertheless, the peak of the mass curve remains a good characterization of the transition from stability to instability. We show that for a configuration with a mass 0.1% away from $M=M_c=0.633$, if it is to the left of the peak in Fig. 3(b), it has the properties of a U -branch star under perturbations, whereas if it is to the right of the peak, it has the properties of an S -branch star, provided small enough perturbations are considered (in particular, the change in mass has to be less than 0.1% in the cases studied). We first consider a configuration with $M=0.632$, $R=5.9$ [$\phi(0)=0.28$]. It is in the left of the peak in Fig. 3(b) on the U branch. Five kinds of perturbations of this configuration have been studied. They are (1) increase ϕ near the center, (2) increase ϕ in the outer region of the star, or (3) change $\dot{\phi}$ (first-type perturbation in Sec. IV D). All these lead to an increase of the density of the star and result in a collapse. (4) Decreasing ϕ near the center or (5) decreasing ϕ in the outer region will result in a migration to the right of the peak in Fig. 3(b). These are the properties of a U -branch star. The evolution for each of the five types of perturbations considered is shown in Fig. 11. The five evolutionary tracks (solid lines) shown are the result of perturbing the initial configuration marked U in the diagram, which is denoted by a box lying on the dashed line representing the locus of equilibria. The tracks labeled $U1$, $U2$, and $U3$ correspond to the first three types of perturbations discussed above. In these tracks the evolution proceeds to the left until a black hole is formed. The tracks labeled $U4$ and $U5$ correspond to

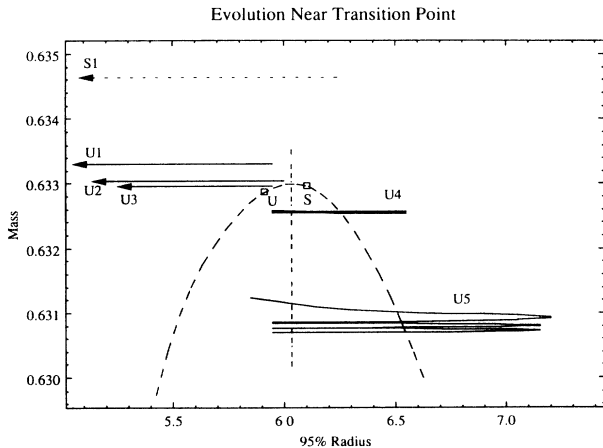


FIG. 11. A detail of Fig. 3(b) near the peak of the mass curve is shown as long dashes with evolutionary tracks overlaid. The U branch (left of peak) and the S branch (right of peak) are separated by a dotted-dashed line at $R=6.03$. The open box marked U is a U branch (unstable) boson star with $M=0.632$, $R=6.1$, $\phi(0)=0.28$, while the open box marked S is a stable boson star with $M=0.63298$, $R=5.9$, $\phi(0)=0.268$. The tracks labeled $U1$, $U2$, and $U3$ are the results of three different types of perturbations (see text for details of perturbations used), all of which increase the mass by very slight amount (all less than 0.1%). These stars collapse rapidly to black holes. The tracks labeled $U4$ and $U5$ are obtained by decreasing the density of the star in the center and in the outer part, respectively, by a very small amount. In these cases, the stars migrate to and oscillate about the S branch. Finally, the track labeled $S1$ is obtained by increasing slightly the density of the initial star marked S . In this case we have perturbed the star enough so that it collapses to a black hole. Taken together, these cases show that under finite perturbations and perturbations that change M and N , there is no exact notion of a transition point, but the peak of the mass curve remains as a useful characterization of the transition from the stable to the unstable branch.

the last two types of perturbations discussed above. The stars migrate to and oscillate about the S branch.

We next consider a configuration with $M=0.63298$, $R=6.1$, and $\phi(0)=0.268$ which is to the right of the peak, on the S branch. The same five kinds of perturbations are studied. With no exception they all lead to oscillation, provided that the perturbation is small. (Any star on the S branch can be made to collapse if enough mass is added to it.) The frequency of the oscillation is $f=0.0014$, independent of the type of perturbation. In fact, this analysis is what produces the lower right most data points in Fig. 6. This configuration clearly belongs to the S branch.

Before we end this subsection, we reiterate that there is no exact notion of a transition point when finite perturbations are considered. The configuration obtained by perturbing the S branch, $M=0.63298$, $R=6.1$ star discussed above, can easily be made to collapse if given a slightly stronger perturbation. The initial, unperturbed configuration is shown as the box marked S in Fig. 11, and its evolution, after its central density was increased by just 2%, is shown as the dashed arrow at the top of the diagram. As in the case of the first three U tracks, this star quickly collapses to a black hole.

V. CONCLUSION

We have developed a numerical code for evolving spherically symmetric self-gravitating scalar field systems. The code is stable and is accurate for a time many orders of magnitude longer than the intrinsic oscillation time scales of the scalar field, and is capable of keeping the Hamiltonian constraint satisfied up to the 10^{-6} level everywhere in the star throughout this time.

In this paper, we reported the results obtained using this code, on the dynamical evolution of a perturbed ground-state boson star. The kinds of perturbations considered include redistribution of scalar particles in the star, and also accretion and annihilation of the scalar particles so that the total mass M and the total number of particles N are not necessarily fixed. We have seen that all equilibrium configurations on the U branch which we have studied exhibit the same behavior when perturbed,

including several configurations with negative binding energy. A U -branch star will either collapse to form a black hole, with practically no scalar radiation out to infinity, or migrate to the S branch, depending on the type of perturbation. When an S -branch star is slightly perturbed, it oscillates with its fundamental frequency. The oscillation is damped through scalar radiation to infinity. This damping mechanism is capable of causing the star to settle down into a new S -branch configuration with lower mass. The damping mechanism is also crucial in making possible the migration of a U -branch star to a S -branch star. This effect could not be seen in a linear analysis. The transition point between the U branch and the S branch has also been studied in detail.

We reiterate the major physical implications of our study on boson star in the astrophysical environment. (i) Existence of boson stars: The S -branch ground-state boson star is stable under generic perturbations. (ii) Signature of a boson star: When perturbed, a boson star oscillates with a frequency characteristic of the final S -branch configuration that it migrates to. (iii) Formation of a boson star: That the scalar radiation by itself is sufficient to drive a scalar field configuration to an S -branch equilibrium configuration, and that both $M > Nm$ and $M < Nm$ configurations in the U branch manage to migrate to the S branch suggest that it might be possible to form a stable boson star under quite general initial conditions.

In future publications in this series, we shall report on the evolution of the excited states of boson stars, boson stars with self-interacting fields, gravitational radiation from nonspherical perturbations,¹⁷ and the formation processes of boson stars.

ACKNOWLEDGMENTS

We would like to thank Andrew Abrahams, Matt Choptuik, David Hobill, Marcello Gleiser, Richard Price, Ian Redmount, Kip Thorne, and Cliff Will for useful discussions. The research was supported in part by NSF Grants Nos. PHY85-13953 and PHY89-06286. The computations were performed on the Cray XMP and Cray YMP under the Grants Nos. NCSA26530 at the National Center for Supercomputing Applications and PHY88-0077P at the Pittsburgh Supercomputing Center.

*Present address.

¹For a review, see, for example, M. S. Turner, in *Fundamental Interactions and Cosmology*, proceedings of the Cargèse Summer School, Cargèse, France, 1984, edited by J. Audouze and J. Tran Thanh Van (Editions Frontières, Gif-sur-Yvette, 1985).

²For a review, see J. R. Primack, D. Seckel, and B. Sadoulet, *Annu. Rev. Nucl. Part. Sci.* **38**, 751 (1988).

³See Ref. 2, and references cited therein.

⁴J. S. Hagelin, G. L. Kane, and S. Raby, *Nucl. Phys.* **B241**, 638 (1984); J. Preskill, M. Wise, and F. Wilczek, *Phys. Lett.* **120B**, 127 (1983); L. Abbott and P. Sikivie, *ibid.* **120B**, 137 (1983).

⁵R. Ruffini and S. Bonazzola, *Phys. Rev.* **187**, 1767 (1969).

⁶M. Colpi, S. L. Shapiro, and I. Wasserman, *Phys. Rev. Lett.* **57**, 2485 (1986).

⁷J. D. Breit, S. Gupta, and A. Zaks, *Phys. Lett.* **140B**, 329 (1984); J. J. van Der Bij and M. Gleiser, *Phys. Lett. B* **194**, 482 (1987); R. Friedberg, T. D. Lee, and Y. Pang, *Phys. Rev.*

D **35**, 3640 (1987).

⁸M. Gleiser, *Phys. Rev. D* **38**, 276 (1988).

⁹P. Jetzer, Fermilab Report No. Conf-88/88-A (unpublished).

¹⁰T. D. Lee, *Phys. Rev. D* **35**, 3637 (1987).

¹¹M. Gleiser and R. Watkins, *Nucl. Phys.* **B319**, 733 (1989).

¹²T. D. Lee and Y. Pang, *Nucl. Phys.* **B315**, 477 (1989).

¹³We have tried various definitions of the radius R [e.g., the position of the peak of g_{rr} or $(4\pi/M) \int \rho r^3 dr$] and find that they give qualitatively the same description.

¹⁴See, for example, J. M. Bardeen and T. Piran, *Phys. Rep.* **96**, 205 (1983).

¹⁵See, e.g., C. W. Misner, K. S. Thorne, and J. A. Wheeler, *Gravitation* (Freeman, San Francisco, 1973).

¹⁶D. H. Bernstein, D. W. Hobill, and L. L. Smarr, *Frontiers in Numerical Relativity* (Cambridge University Press, Cambridge, England, 1989).

¹⁷E. Seidel, E. Myra, and T. Moore, *Phys. Rev. D* **38**, 2349 (1988).